The Pennsylvania State University
The Graduate School
College of Engineering

AUTOMATIC CONTROLLER SYNTHESIS FOR A RECONFIGURABLE UAV

A Thesis in
Aerospace Engineering
by
Joseph D. Harkins

Submitted in Partial Fulfillment
of the Requirements
for the Degree of

Master of Science

August 2017

The thesis of Joseph D. Harkins was reviewed and approved* by the following:

Jacob W. Langelaan
Associate Professor of Aerospace Engineering
Thesis Advisor

Michael A. Yukish
Assistant Professor of Aerospace Engineering

George A. Lesieutre
Professor of Aerospace Engineering
Acting Head of the Department of Aerospace Engineering

*Signatures are on file in the Graduate School.

Abstract

This thesis describes the development of an adaptable control architecture that can be used to automatically synthesize inner-loop controllers for new configurations of modular aircraft. This will allow for new configurations to be flown without the need for extensive flight testing to tune the controller gains for favorable flying characteristics. This is achieved by breaking the aircraft geometry into finite strips and calculating the forces and moments on each strip using 2D airfoil approximations. The contributions of each finite strip are then summed to obtain the approximate equations of motion for the aircraft. These equations are then linearized about a cruise setpoint. This linearized dynamics model for the aircraft is then used to synthesize inner-loop controllers for roll, pitch, and yaw. These controllers can be implemented within an on-board autopilot system, therefore enabling autonomous flight 'out of the box'. The performance of these controllers was simulated and compared to controllers generated using an established vortex-lattice code to determine the accuracy of the finite strip method.

Table of Contents

List of Figures

List of Tables

List of Symbols

a	Lift curve slope of a finite wing
a_0	Lift curve slope of an infinite wing
AR	Aspect Ratio
b	Wing span
c	Wing chord
C_D	Drag coefficient
C_{D_0}	Profile drag coefficient
C_L	Lift coefficient
C_{L_0}	Zero angle of attack lift coefficient
C_{L_α}	Lift curve slope
C_{L_δ}	Change in C_L with δ
C_{l_p}	Non-dimensional stability derivative of roll moment with roll rate
$C_{l_{\delta_a}}$	Non-dimensional stability derivative of roll moment with aileron deflection
C_M	Moment coefficient
C_{M_0}	Average moment coefficient
C_{M_δ}	Change in C_M with δ
C_{m_q}	Non-dimensional stability derivative of pitch moment with pitch rate

$C_{m_{\delta_e}}$	Non-dimensional stability derivative of pitch moment with elevator deflection
C_{n_r}	Non-dimensional stability derivative of yaw moment with yaw rate
$C_{n_{\delta_r}}$	Non-dimensional stability derivative of yaw moment with rudder deflection
e	Span efficiency
F	Force
g	Gravitational acceleration
I_x	Moment of inertia about x-axis
I_y	Moment of inertia about y-axis
I_z	Moment of inertia about z-axis
K_I	Integral controller gain
K_P	Proportional controller gain
L	Aerodynamic moment about x-axis (roll moment)
L'	Lift per unit span
M	Aerodynamic Moment about y-axis (pitch moment)
m	Aircraft mass
N	Aerodynamic moment about z-axis (yaw moment)
P	Roll rate
Q	Pitch rate
R	Yaw rate
$\mathbf{r}$	Location vector
S	Wing area
s_i	Panel length
u	Velocity in x-direction
V	Velocity

v	Velocity in y-direction
w	Velocity in z-direction
X	Aerodynamic force in x-direction
$\hat{X}$	X-direction
Y	Aerodynamic force in y-direction
$\hat{Y}$	Y-direction
Z	Aerodynamic force in z-direction
$\hat{Z}$	Z-direction
α	Angle of attack
β	Angle of sideslip
Γ	Total vortex strength
γ_i	Discretized vortex strength
Δ	Disturbance value
δ	Control surface deflection angle
δ_a	Aileron deflection angle
δ_e	Elevator deflection angle
δ_r	Rudder deflection angle
θ	Pitch angle
ξ	Damping ratio
ρ	Air density
$\sum$	Summation
ϕ	Roll angle
ψ	Yaw angle
$\boldsymbol{\omega}$	Angular velocity vector

ω_n	Natural frequency
$(*)^b$	In the body reference frame
$(*)^E$	In the Earth reference frame
$(*)^i$	In the section reference frame
$(*)_b$	Of the aircraft
$(*)_i$	Of the segment
AM	Additive Manufacturing
AVL	Athena Vortex Lattice
CFD	Computational Fluid Dynamics
CG	Center of Gravity
EoM	Equation of Motion
FDM	Fused Deposition Modeling
SLM	Selective Laser Melting
SLS	Selective Laser Sintering
UAV	Uninhabited Air Vehicle

Acknowledgments

I would like to thank my advisor, Jack Langelaan, for his advice and assistance throughout the process of completing this thesis as well as during the extent of my graduate career at Penn State.

I would like to thank my co-workers at the Penn State Applied Research Lab for their support and guidance throughout my time at Penn State.

Lastly I would like to thank my family for continually providing support and advice, which has helped me reach this point in my career despite numerous roadblocks and detours.

Chapter 1

Introduction

This thesis describes the development of a control architecture for reconfigurable uninhabited air vehicles (UAVs). The intent was to develop a control architecture that can automatically detect aircraft configuration and synthesize controllers. This allows for a controller that can be quickly and easily adapted to new aircraft configurations. This should then allow the aircraft to fly autonomously without the need to tune the controller gains for each new configuration. This can be vital in situations where time is not available for a full flight test regime to be run before a mission.

1.1 Research Motivation

As additive manufacturing (commonly known as 3D Printing) becomes more commonplace, with relatively low-cost (<$600 in 2017) printers widely available, the use of AM in the manufacture of air vehicles is increasing[13][1][17]. This trend will continue as prices drop, material properties improve, and build speed and volume increases. The benefit of AM is the ability to create structures of extreme complexity that would be impossible to manufacture using conventional methods. This allows for new designs that can maximize strength and usable interior space, while also minimizing weight. While most consumer 3D printers use plastic as the building material, metals and composites are also available to be used with some industrial printers. Several build methods are used by different printers depending on the material used and the cost of the machine. The cheapest and most common

Printer	Cost	Manufacturer	Build Method	Build Material	Build Volume (mm)
Original Prusa i3 MK2[11]	$699	Prusa Research	FDM	Plastic	250 x 210 x 200
Replicator Mini+[12]	$1,299	MakerBot	FDM	Plastic	102 x 127 x 127
Makergear M2[11]	$1,825	Makergear	FDM	Plastic	254 x 203 x 203
Fortus 900mc[21]	$250,000	Stratasys	FDM	Plastic	914 x 610 x 914
EOS P 396[11]	$250,000	EOS	SLS	Plastic, Metal	340 x 340 x 600
X Line 2000R[6]	$1,600,000	Concept Laser	SLM	Metal	800 x 400 x 500

Table 1.1: Examples of commercially available 3D printers

build method for plastics is Fused Deposition Modeling (FDM), which involves liquefying the plastic and extruding it onto a build platform to construct the desired shape for each layer. A more expensive method used for plastics, metals, as well as a variety of other materials is Selective Laser Sintering (SLS). This method involves using a laser to melt and solidify the powdered source material in the desired shape for each layer. A similar method to SLS called Selective Laser Melting (SLM) uses a laser to completely melt metal powder such that is solidifies into a completely solid homogeneous part [18]. A list of some examples of different types, sizes, and prices of 3D printers is shown in Table 1.1.

One of the biggest drawbacks of current 3D printers is the limited build volume, which restricts the maximum size of components that can be manufactured. What this results in, with respect to 3D printing aircraft, is either limiting the overall size of the printed vehicle, or breaking up the structure into smaller modules that can then be assemble together into an aircraft.

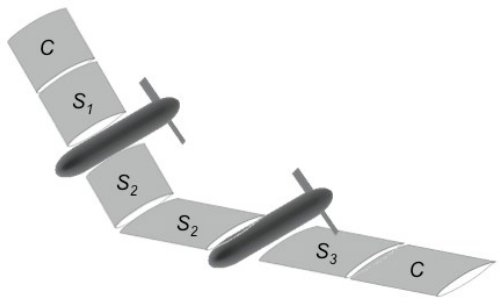

Figure 1.1: Example of modular aircraft configuration

The key advantage of AM is that custom parts can be made on-site and tailored to specific design requirements. Within the context of UAVs, an operator could specify a mission (e.g. carry a sensor payload of given size and mass over a given distance and circle a location for a given time) and have an aircraft automatically generated that can fly the mission. Critical design parameters include wing area, wing span, and required power; constraints include payload size, weight, available power, required endurance, and required range. This thesis considers on-demand additive manufac-

turing of a UAV using a limited build volume 3D printer. In this context, the UAV will consist of multiple 3D printed modules that are assembled to form the complete vehicle. An example of a modular aircraft configuration is shown in Figure 1.1, where C represents a common section that is universal for any configuration and S represents a configuration specific section. These configuration specific sections could contain a payload, batteries, sensors, or control surfaces. To successfully design an AM aircraft, aircraft design has to be closely coupled to manufacturing design. The manufacturing design ensures that the aircraft can be successfully built using a given printer's build volume and material constraints. The aircraft design must then take these constraints and determine a viable configuration for the given mission. The number of adjustable parameters available has the ability to produce a large quantity of aircraft configurations that meet the required constraints. However, not all of these configurations will be viable, the majority will be either aerodynamically unstable or have unfavorable handling characteristics. Designing and testing a controller for each of the configurations to determine viability is not practical. Thus a method is needed that can automatically determine aerodynamic stability and controllability in-line with the design process, this thesis describes such a method. The example aircraft used in this thesis were designed to be manufactured on a Fortus 450mc, with the constraints of using ULTEM plastic aiming to minimize the use of internal support material and a build volume of 16" x 14" x 16". A CAD model of an example aircraft is shown in Figure 1.2. The variable design parameters for this family of aircraft are, the number of wing segments (3, 5, or 7), the number and location of motor assemblies (from one up to the total number of wing segments), the number and location of tail assemblies (from two up to the total number of wing segments), and the size and location of the payload. These design parameters result in a large number of possible configurations that would be impractical to work with. This motivates the desire to autogenerate controllers to help eliminate non-viable configurations.

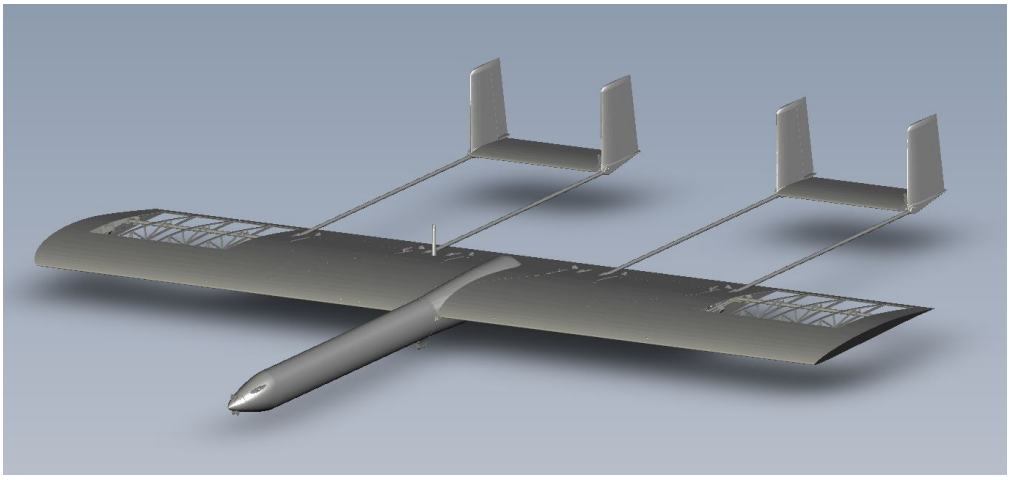

Figure 1.2: CAD model of example UAV configuration

One of the potential uses of the technology and methods developed for this project is for a front-line UAV that can be outfitted with various sensor packages and perform various mission profiles. In the field access to engineers able to reconfigure the aircraft for these differing mission profiles and air-frame geometries is limited or non-existent. Therefore having a system that can determine aircraft geometry for you as well as write the control laws that permit autonomous flight given the specific mission and payload can be vital to mission success.

In order to successfully implement this system several technical challenges related to the flight vehicle design need to be addressed. Aerodynamics, structures, propulsion, and flight control are the key components of flight vehicle design and must each be given equal attention. This thesis focuses on the flight control aspect, specifically in the development of a control architecture that can automatically synthesize controller gains for a given configuration. In this thesis the controller synthesis problem is further constrained to focus on inner loop control, i.e., control of roll, pitch, and yaw rates.

1.2 Control Law Synthesis for Modular Aircraft

In order to better understand the effect a change in the aircraft's geometry will have on the control law for that aircraft it is necessary to understand how the controller works. Shown in Figure 1.3 is a block diagram representation of a system with a feedback controller implemented . The plant G(s) represents the dynamics

of the system, in this case the dynamics of the aircraft. The output of the plant is fed back and compared to the commanded reference condition (e.g., pitch angle). The difference between the output from the dynamics and the reference input is the error for that particular variable. The error is the input to the controller K(S) which has dynamics such that the output from the controller is the required control input to the plant dynamics (e.g., elevator deflection) in order to bring the error to zero.

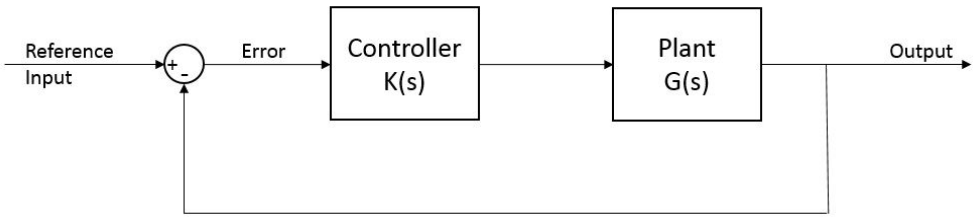

Figure 1.3: Block diagram of system with controller

A controller is designed to work optimally with a specific plant model. Therefore changes to the plant model require changes to the controller or else the system could become unstable/uncontrollable. The addition of components to a modular aircraft will in general cause significant changes to the aircraft's dynamics. For example if an additional wing segment is added there could be an effect on weathercock and roll stability and may also affect higher level controls such as cruise speed. In addition, the extra wing segment may alter other stability and control derivatives enough to affect controller performance. While these changes won't necessarily affect the stability or controllability of the aircraft, they must be accounted for when designing the controller to ensure optimal performance.

Classical control techniques such as PID control, which are still in use in a wide array of manned and unmanned aircraft, including the Pixhawk autopilot system used in this thesis, require reasonably accurate flight dynamics models to function properly. The next step is to come up with a method to accurately model aircraft dynamics that is easily adaptable to different module configurations. The technique used in this thesis to determine this dynamic model for an arbitrary aircraft configuration involves breaking the aerodynamic surfaces of the aircraft into discrete strips. These strips are treated as 2D airfoils in order to calculate their aerodynamic coefficients, i.e., lift, drag, and moment coefficients. Using the

aerodynamic coefficients, the forces and moments for each strip are summed to get the overall equations of motion (EoMs) for the aircraft. This method is henceforth referred to as the 'strip model'.

1.3 Pixhawk Autopilot

The research in this thesis is done assuming the use of a Pixhawk autopilot system. The Pixhawk is an open-source autopilot hardware module suitable for most mobile robotics platforms, land, sea, or air. The hardware module, shown in Figure 1.4, contains the main processor for the vehicle that the autopilot software is loaded to. The hardware module also contains the basic required sensors, a 3D accelerometer, gyroscope, magnetometer, and barometer, as well as connection ports for other sensors that may be needed (e.g., GPS, airspeed, etc)[15]. There are two autopilot software 'flight stacks' that can be used with the Pixhawk, the ArduPilot[4] and PX4[16] open-source autopilot flight stacks.

Figure 1.4: Pixhawk Hardware Module[15]

This thesis uses the PX4 autopilot software as the basis for the control architecture development. The PX4 autopilot uses PI controllers for the inner-loop angular rate controllers, which will be the focus of the controller development presented in Chapter 4. Figure 1.5 shows a block diagram schematic of the pitch control loop used in the PX4 autopilot. The control scheme consists of an inner PI controller around the pitch rate with a pitch angle proportional controller wrapped around it. The outermost loop shows an airspeed hold controller, however this could change depending upon the mode the autopilot is in. In airspeed or altitude hold mode the respective controller is applied in the outer-loop, while for stabilized manual mode the pilot's input goes straight to the pitch angle command.

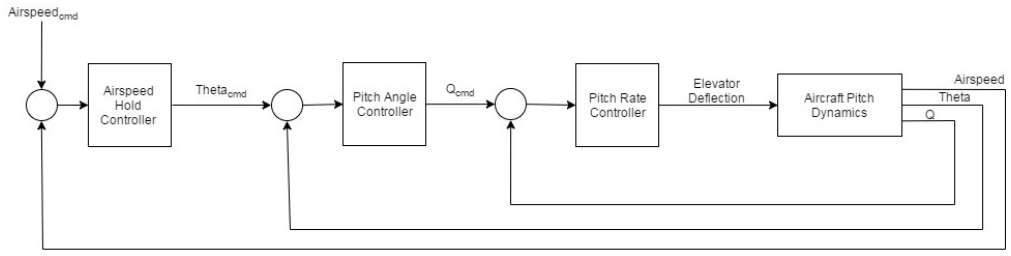

Figure 1.5: PX4 Autopilot Pitch Control

1.4 Related Work

There are two main fields of research that relate to the work done in this thesis: aerodynamic modeling of flight vehicles and control synthesis. The relevant aerodynamic modeling background is mainly vortex lattice methods (used here to verify the main approach) and blade element theory. In this thesis, controller synthesis is done in a manner intended to be consistent with the control architecture on a commercially available autopilot unit (the Pixhawk autopilot with PX4 flight software).

1.4.1 Aerodynamic Modeling of Flight Vehicles

The method used to develop the strip model is very similar to blade element theory, which is commonly used to predict the performance of propellers, fans, or wind turbines. Blade element theory involves dividing a propeller blade into discrete independent sections. 2D airfoil properties are then used to obtain a force balance, which when coupled with a momentum balance yields a set of non-linear coupled equations. These non-linear equations are solved by iteration to obtain the contribution of that particular section. The components from each section are then summed to obtain the overall thrust and torque provided by that propeller blade[5]. A depiction of the blade discretization can be seen in Figure 1.6. An illustration of the forces and velocities on an individual element can be seen in Figure 1.7. V_0 is the axial flow experienced by the propeller (aircraft forward speed in most cases). V_1 is the velocity due to the angular rotation of the propeller. θ is the geometric pitch angle of the blade element and α is the effective angle of attack seen by the blade element. While this method contains non-linearities that require solving through iteration, the strip model described in Chapters 2 and 3 is

linearized so that (assuming small perturbations) the forces and moments can be resolved directly.

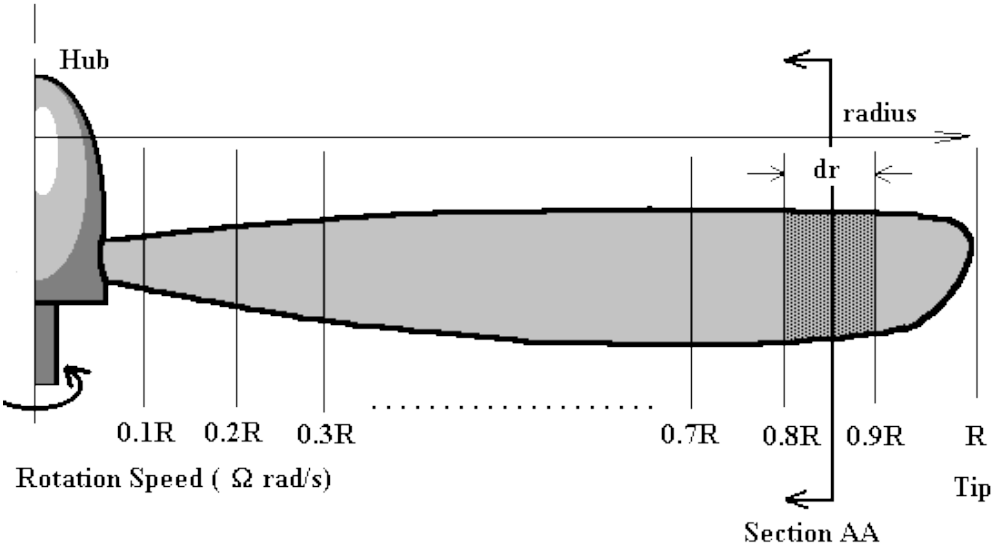

Figure 1.6: Blade Element Theory Discretization[5]

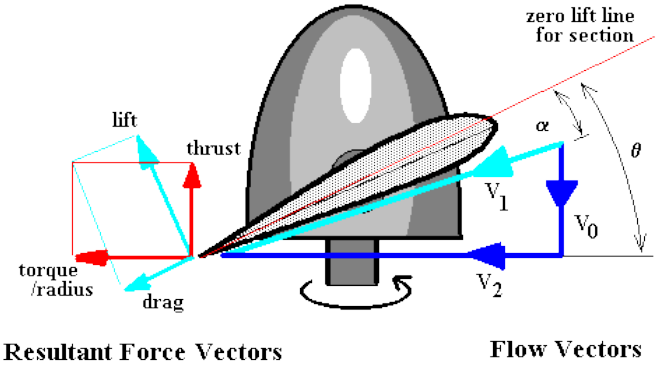

Figure 1.7: Blade Element Theory Elemental Forces[5]

Selig[19] discusses using a strip model based on blade element theory to model wing aerodynamics within a real-time simulation. The method uses look-up tables calculated with a nonlinear lifting-line code to get aerodynamic properties of each discrete section. Combined with contributions from other surfaces the forces and moments on the aircraft can be resolved in real time. This allows for an accurate aerodynamic model of the aircraft even in highly nonlinear flight regimes.

Typically blade element theory uses the vortex panel method to calculate the performance of 2D airfoils. The commercial panel code used to predict airfoil performance in this thesis was Xfoil[8]. The idea behind the vortex panel method is to discretize the 2D airfoil into separate 'panels' of length s_i. At the center of each panel is a control point with a vortex of unknown strength γ_i. A depiction of this vortex distribution is shown in Figure 1.8.

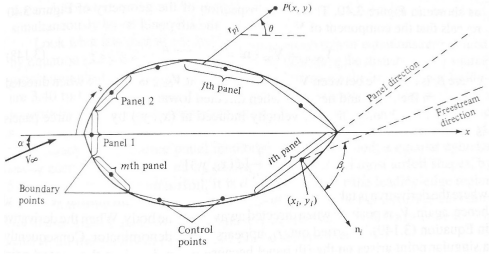

Figure 1.8: Panel Method Vortex Distribution[3, p. 285]

The point P is an arbitrary point at which the contribution from each vortex can be summed to get the total velocity potential at that point. When P is at a control point a boundary condition of zero normal velocity is applied. When that boundary condition is applied to all control points around the airfoil it creates a streamline along the surface of the airfoil. The boundary condition at each control point coupled with the contributions of all other vortices on a given control point leads to a system of n equations and n unknowns, where n is the number of panels and the unknowns are the individual vortex strengths. This system of equations can then be solved resulting in the values for the panel vortex strengths γ_i. The total lift on the airfoil can then be found by

$$L' = \rho_\infty V_\infty \sum_{i=1}^{n} \gamma_i \, s_i \tag{1.1}$$

where L' is the lift per unit span of the airfoil and ρ_∞ and V_∞ are the density and velocity of the air stream[3, pp. 361-365].

The most common way to model aircraft aerodynamics is to use vortex lattice method to create a linear dynamics model. The vortex lattice code used to obtain the baseline aerodynamic models in this thesis was AVL[7]. Vortex lattice works in a similar vein to the vortex panel method, except instead of panels around the surface of an airfoil, the vortices are applied in horseshoe shaped sheets to the entire surface of a given lifting surface. A similar boundary condition is also applied, in that the normal component of the velocity induced by all the other vortices should

be zero at any point on the lifting surface. A depiction of a lifting surface, covered by this vortex sheet is shown in Figure 1.9. Once again a system of simultaneous algebraic equations is obtained and can be solved to get the lift distribution over the wing[3, pp. 457-462].

Park[14] shows the use of vortex lattice method in determining the aerodynamic model of a small UAV. The frequency response of this model is then compared to flight test data. The results show that the vortex lattice linear model roughly predicts aircraft performance and can be fine-tuned with flight test data.

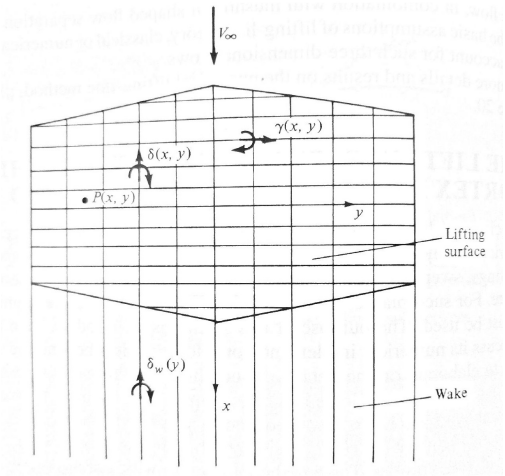

Figure 1.9: Vortex Lattice Vortex Distribution[3, p. 458]

Another method for simulating aircraft aerodynamics is computational fluid dynamics (CFD), which uses finite difference to solve the Navier-Stokes equations in the flow-field surrounding the aircraft. A detailed explanation of the Navier-Stokes equations can be found in [3, pp. 908-911]. Since the finite difference method requires iteratively solving the equations at every point in the flow-field it is very computationally expensive. For this reason it is typically used as a validation tool for aerodynamic models created by other means, rather than to directly create a model. Murphy et al.[2] use CFD simulation and wind tunnel data to create a linear aerodynamic model of an aircraft in an oscillatory roll by estimating the unknown parameters using harmonic analysis and two-step linear regression. In this case the CFD data was used to augment the wind tunnel data for conditions that were not tested.

1.4.2 Controller Synthesis

There is currently not a lot of published research in the area of modular unmanned aerial vehicles and developing control laws for them. There is a much more significant amount of research being done on adaptive control systems for the

purpose of reacting to control surface loss or airframe damage. That research is primarily on a reactionary control system for adapting to changes in-flight rather than being able to quickly adapt the control system to completely different aircraft geometries in the field.

Forte et al.[10] studied a modular UAV system consisting of n number of tail-sitting ducted-fan air vehicles configured arbitrarily. The foundations for the calculations of the system's equations of motion are very similar to those presented in this thesis. They performed a force and moment balance on each air vehicle and then using the individual component's location and orientation respective to the center of gravity of the formation, formed the dynamic model of the entire system. They then used this dynamic model to construct a controller for the system that stabilizes the vehicle about a set-point.

Zhang et al.[22] look at a different way to solve a similar problem as is presented in this thesis. The seek to use immersion and invariance based estimation and adaptive backstepping control to create a controller that requires no previous knowledge of some of the aerodynamic properties of the aircraft. The immersion and invariance estimator calculates an estimate of the unknown parameter using both a partial estimate based off of a dynamics update law as well as a prescribed non-linear function. The update law is chosen such that the estimation error dynamics have an equilibrium at zero error, and the non-linear function is chosen such that the dynamics are stable. The backstepping controller creates an intermediate control law designed to render the closed-loop system stable to perturbation inputs and estimator error. The result is a functional aircraft pitch controller that is stable without knowing the longitudinal damping characteristics of the aircraft.

This work, while relevant to the topic discussed in this thesis, is not directly applicable and therefore a new method needs to be created. Forte's model is for a set of individual UAVs connected together each with one control (thrust). Since surfaces on a fixed wing aircraft can have multiple controls, or none at all, while significantly affecting the vehicle's dynamics, this method is not sufficient. Zhang's method is much more complex and computationally intense, therefore not suitable for calculating controllers for numerous configurations. In addition, the configurations can be vastly different and therefore attempting to estimate the variable parameters around a baseline may not yield a valid result.

1.5 Theoretical Background

The strip model uses several theoretical models in order to accurately predict aerodynamic performance while also maintaining computational simplicity. Some of these theories are extensions of, or incorporate some of the more fundamental theories of aerodynamics. The main theoretical models that serve as the foundational basis of the strip model are the Prandtl lifting-line theory and small disturbance theory.

1.5.1 Prandtl Lifting-Line Theory

Ludwig Prandtl's lifting-line theory was the first practical theory used to predict the lift generated by a finite wing. The theory supposes that a finite wing can be replaced with a fixed bound vortex the same width as the span of the wing. From the Kutta-Joukowski theorem this bound vortex will experience a lift per unit span of $L' = \rho_\infty V_\infty \Gamma$ where Γ is the strength of the bound vortex. From Helmholtz's theorem this vortex filament cannot end within the fluid. To avoid this the vortex filament continues as two infinite free vortices traveling downstream from the wingtips. The bound vortex and the two free vortices are known as a horseshoe vortex. A depiction of a horseshoe vortex is shown in Figure 1.10.

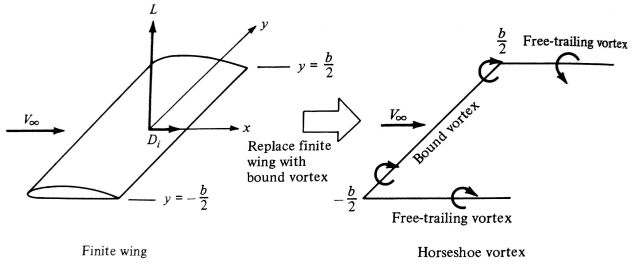

Figure 1.10: Finite Wing Modeled as a Horseshoe Vortex[3, p. 424]

This single horseshoe vortex unfortunately does not accurately represent a real finite wing. The solution that Prandtl's theory states, is to superimpose an infinite number of these horseshoe vortices each with a differential strength of $d\Gamma$. A depiction of the superposition of the horseshoe vortices is shown in Figure 1.11. The strengths of these vortices can be integrated over the span of the wing to get the vortex strength as a function of distance along the span. The lift distribution

can be obtained by applying the Kutta-Joukowski theorem. This lift distribution is integrated over the entire span to get the total lift produced by the wing[3, pp. 424-429].

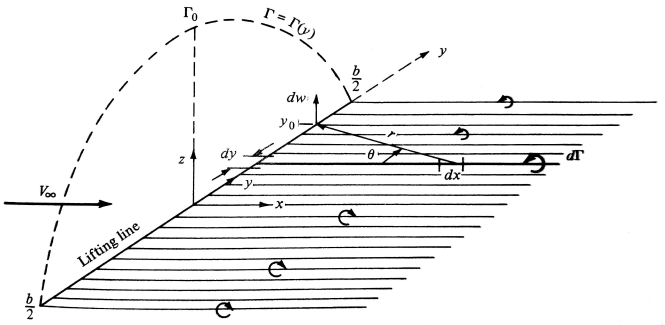

Figure 1.11: Superposition of an Infinite Number of Horseshoe Vortices[3, p. 427]

The primary result from this theorem used in the creation of the strip model is the relationship it derives between the infinite wing lift curve slope and the finite wing lift curve slope. This relationship, for a wing with a general lift distribution, is

$$a = \frac{a_0}{1 + \frac{a_0}{\pi e AR}} \tag{1.2}$$

where a is the lift curve slope of the finite wing, a_0 is the lift curve slope of the infinite wing, AR is the aspect ratio of the finite wing, and e is the span efficiency[3, p. 443]. The span efficiency is a function of the wing planform shape. This relationship is useful for the strip model because it allows the 2D airfoil aerodynamic data to be modified to better reflect the actual aerodynamic performance of the 3D wing.

1.5.2 Small Disturbance Theory

Small disturbance theory is used primarily as a method for approximating non-linear systems as linear. This is useful because linear systems are much easier to solve and often have a closed-form solution. Non-linear systems, with the exceptions of a few special cases, do not have closed-form solutions and must use computationally expensive numerical methods to solve. Small perturbation theory states that any set of non-linear functions can be approximated by a set of linear functions given that the state variables are subject to small deviations from a steady flight reference condition, and that the functions and their derivatives are continuous. The linear

function is given by a Taylor Series expansion of the non-linear function evaluated at a reference point. The expansion, $\Delta F(x) = F(x_0) + \frac{dF}{dx}\Big|_{x_0} \Delta x + \frac{dF^2}{d^2x}\Big|_{x_0} (\Delta x)^2 + \ldots$ is then truncated to a first order approximation which, as long as the function and its first derivative are continuous, is a valid linear approximation. The function then becomes a simple first order equation based on the value of the function at the reference point plus the disturbance value of the state variable multiplied by the derivative of the function with respect to that variable evaluated at the reference point. This method can also be expanded to functions dependent on several variables by doing the Taylor Series approximation with respect to each variable and then summing the resulting components to get the total change in the function due to the disturbances in its state variables[9, pp. 109-110].

1.6 Potential Applications

The main potential application for this strip model would be to embed it in an on-board flight computer that connects to microprocessors in each section. These microprocessors would know if they have a control surface at their location, as well as their relative location within the aircraft. The flight computer takes these data, as well as preprogrammed knowledge of the geometry of the modular components, and creates an input to the strip model of the current aircraft configuration. The strip model is used to determine the controller gains necessary to autonomously fly that configuration. These gains are written to a parameter file readable by the autopilot and uploaded to the autopilot hardware. This will allow for 'plug-and-play' adaptability of the system. If a new type of mission is needed and requires a different configuration, the required modules and surfaces are assembled, the flight computer identifies the configuration change and writes new controller gains to the autopilot, then the aircraft is ready to fly.

Another application would be in re-configuring the aircraft controller in case of actuator failure or airframe damage. Sensors embedded in the control surfaces and within the aerodynamic surfaces would send a signal to a central computer. A failure of a control surface or the loss of an aerodynamic surface could would lead the computer to run the strip model for all remaining/functioning surfaces and rewrite the control laws to allow the aircraft to maintain control and land safely.

The simple and computationally inexpensive strip model would also be able to

be embedded within configuration optimization software. This will allow for the rejection of unstable cases without the need to run a vortex lattice simulation for each configuration. This has the potential to drastically reduce the computation time of the optimization software as well enable the use of more parameters in the optimization. Examples of extra parameters that could be included are

- Wing dihedral/twist angles
- Tail configurations (e.g. V-Tail, H-Tail, T-Tail, etc.)
- Airfoil shape
- Control surface type

1.7 Reader's Guide

The rest of this thesis is organized as follows

- Chapter 2 describes the problem and the fundamental concepts used to solve it.
- Chapter 3 details the creation of the linear aerodynamics model for an arbitrarily configured aircraft as well as the underlying assumptions used to create this model. The chapter ends with the linearized equations of motion of a generic aircraft in terms of its stability and control derivatives.
- Chapter 4 derives the control laws used for the aircraft as well as the equations for the controller gains in terms of the stability and control derivatives.
- Chapter 5 shows the validation of the strip model with respect to the vortex lattice method and shows the comparison of the controller response between them.
- Chapter 6 discuses the overall results of this thesis as well as the conclusions that can be drawn from them. The chapter also describes possible sources of error and potential future work.

Chapter 2

Problem Definition

The crux of the problem this thesis attempts to solve is how to get a closed-form solution for an aircraft's equations of motion that can be applied to a multitude of aircraft configurations. A closed-form solution, dependent only upon known parameters, allows the equations of motion to be determined instantly. With these equations of motion, the stability and relative contollability of the aircraft become known. In addition, the inner-loop controller gains necessary for autonomous flight can be calculated. The method used to calculate the controller gains begins with breaking the aircraft's aerodynamic surfaces into individual sections. The main wing is broken up into discrete sections and grouped together for the purpose of finite wing corrections, and then all remaining aerodynamic surfaces are treated as individual sections and put into another group. Each individual section is then treated as a 2D airfoil, the forces and moments acting on each individual section are calculated in terms of the section's geometry, 2D aerodynamic coefficients, location, as well as the velocity and angular rates of the global aircraft. These equations of motion are calculated with respect to the section's local coordinate frame. Once these force and moment equations are obtained for an individual section, a coordinate transform is used to obtain that section's contribution to the total forces and moments in the global aircraft coordinate frame.

2.1 Coordinate Frames and Equations of Motion

The aircraft's body coordinate frame is defined in the traditional sense, with the origin at the center of gravity (CG), the X-axis out the nose, Y-axis out the right wing, and Z-axis down. A depiction of the aircraft body frame is shown in Figure 2.1. The body frame is defined with respect to an inertial frame located at an arbitrary point on the Earth's surface. Assuming a flat-earth model, the X, Y, and Z axes of the inertial frame are defined in the North, East, and Down directions respectively. The location of the body frame is given by a vector $\mathbf{r}^E$ and its orientation is defined by the Euler angles ψ^E, θ^E, and ϕ^E. Standard Euler angle definitions are used, such that

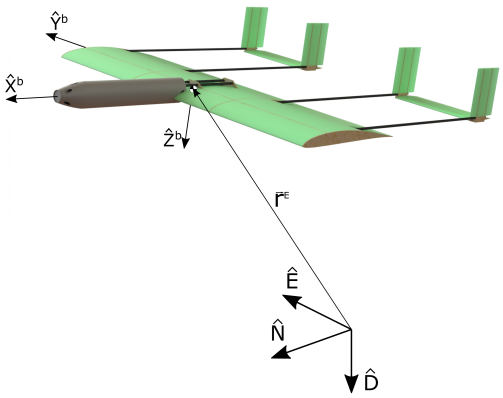

Figure 2.1: Aircraft Body Frame

$$\mathbf{x}^b = \begin{bmatrix} \mathrm{c}\theta\,\mathrm{c}\psi & \mathrm{c}\theta\,\mathrm{s}\psi & -\mathrm{s}\theta \\ -\mathrm{c}\phi\,\mathrm{s}\psi \;+\; \mathrm{s}\phi\,\mathrm{s}\theta\,\mathrm{c}\psi & \mathrm{c}\phi\,\mathrm{c}\psi \;+\; \mathrm{s}\phi\,\mathrm{s}\theta\,\mathrm{s}\psi & \mathrm{s}\phi\,\mathrm{c}\theta \\ \mathrm{s}\phi\,\mathrm{s}\psi \;+\; \mathrm{c}\phi\,\mathrm{s}\theta\,\mathrm{c}\psi & -\mathrm{s}\phi\,\mathrm{c}\psi \;+\; \mathrm{c}\phi\,\mathrm{s}\theta\,\mathrm{s}\psi & \mathrm{c}\phi\,\mathrm{c}\theta \end{bmatrix} \mathbf{x}^E \tag{2.1}$$

where $\mathrm{c}(\cdot) = \cos(\cdot)$ and $\mathrm{s}(\cdot) = \sin(\cdot)$[20, p. 26].

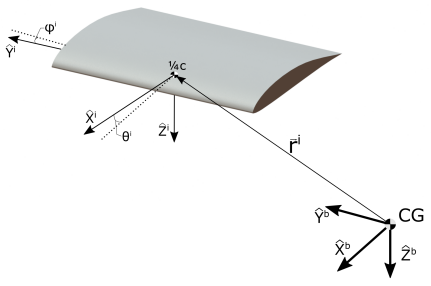

Figure 2.2: Section Coordinate Frame

The local coordinate frame of an arbitrary section is defined with its origin located mid-span at the quarter-chord point. The X-axis is defined out the leading edge of the section, the Y-axis out the right edge of the section, and the Z-axis out the bottom. The location of the local coordinate frame with respect to the body frame is given by the location vector $\mathbf{r}_i^b$. The orientation of the local frame with respect to the body frame is defined by the angles θ_i

and ϕ_i which define the section's orientation with respect to $\hat{Y}^b$ and $\hat{X}^b$ respectively. A depiction of an arbitrary section coordinate frame and its relation to the body frame is shown in Figure 2.2.

The key equations of motion of an aircraft, assuming an XZ plane of symmetry and a body frame aligned with the aircraft's principle axes, are

$$X - m\,g\sin\theta^E = m\,(\dot{u} + Q\,w - R\,v) \tag{2.2}$$

$$Y + m\,g\cos\theta^E\sin\phi^E = m\,(\dot{v} + R\,u - P\,w) \tag{2.3}$$

$$Z + m\,g\cos\theta^E\cos\phi^E = m\,(\dot{w} + P\,v - Q\,u) \tag{2.4}$$

$$L = I_x\dot{P} - (I_y - I_z)\,Q\,R \tag{2.5}$$

$$M = I_y\dot{Q} - (I_z - I_x)\,R\,P \tag{2.6}$$

$$N = I_z\dot{R} - (I_x - I_y)\,P\,Q \tag{2.7}$$

These assumptions allow any terms including the products of inertia, I_{xy}, I_{xz}, and I_{yz}, to be dropped[9, p. 101]. Here m is the mass of the aircraft, the I's are the moments of inertia, and g is the acceleration due to gravity. The components of the aircraft's velocity through the air are given by u, v, and w, and it's angular velocities by P, Q, and R All of these quantities are known for a given aircraft in a given flight condition. Therefore the quantities of interest for characterizing the motion of an aircraft are the aerodynamic forces and moments (X, Y, Z, L, M, and N). The remainder of this chapter discusses the method used calculate these forces and moments by discretizing the aircraft's aerodynamic surfaces into finite strips, calculating the forces and moments on each individual strip, and then summing all contributions together to get the total forces and moments acting on the aircraft.

2.2 Forces and Moments on i^{th} Section

Consider an arbitrary section as depicted in Figure 2.2. To calculate the aerodynamic forces and moments acting on this section, first the relative wind acting on the section must be determined. This relative wind vector (with components u_i^i, v_i^i, and w_i^i) is computed using the aircraft's velocity components (u_b^b, v_b^b, and w_b^b), angular rates

$$\boldsymbol{\omega}_b^b = \begin{bmatrix} P \\ Q \\ R \end{bmatrix}$$

as well as the location vector of the section

$$\mathbf{r}_i^b = \begin{bmatrix} r_{x,i} \\ r_{y,i} \\ r_{z,i} \end{bmatrix}$$

The local velocity vector in the aircraft body frame is given by

$$\begin{bmatrix} u_i^b \\ v_i^b \\ w_i^b \end{bmatrix} = \begin{bmatrix} u_b^b \\ v_b^b \\ w_b^b \end{bmatrix} + \boldsymbol{\omega}_b^b \times \mathbf{r}_i^b = \begin{bmatrix} u_b^b \\ v_b^b \\ w_b^b \end{bmatrix} + \begin{bmatrix} r_{z,i}Q - r_{y,i}R \\ r_{x,i}R - r_{z,i}P \\ r_{y,i}P - r_{x,i}Q \end{bmatrix} \tag{2.8}$$

Using Equation 2.9 the local velocity vector for the section then is transformed from the aircraft body coordinate frame to the local coordinate frame of the individual section. This enables easier calculation of the aerodynamic forces on the section since lift and drag are in local $\hat{X}^i$ and $\hat{Z}^i$ directions which are not necessarily the same as the global $\hat{X}^b$ and $\hat{Z}^b$.

$$\begin{bmatrix} u_i^i \\ v_i^i \\ w_i^i \end{bmatrix} = \mathbf{T}_{i/b} \begin{bmatrix} u_i^b \\ v_i^b \\ w_i^b \end{bmatrix} \tag{2.9}$$

The transformation matrix $\mathbf{T}_{i/b}$, used to transform a vector from the body frame to the local coordinate frame of the i^th section, is an Euler angle transformation using only pitch and bank and is given by

$$\mathbf{T}_{i/b} = \begin{bmatrix} \cos\theta_i & 0 & -\sin\theta_i \\ 0 & 1 & 0 \\ \sin\theta_i & 0 & \cos\theta_i \end{bmatrix} \begin{bmatrix} 1 & 0 & 0 \\ 0 & \cos\phi_i & \sin\phi_i \\ 0 & -\sin\phi_i & \cos\phi_i \end{bmatrix} \tag{2.10}$$

Here θ_i is the rotation of the i^th segment about the body y-axis and ϕ_i is a rotation about the segment's resulting x-axis.

The section angle of attack and angle of sideslip in the local coordinate frame are

$$\alpha_i = \arctan(\frac{w_i^i}{u_i^i}) \tag{2.11}$$

$$\beta_i = \arctan(\frac{v_i^i}{u_i^i}) \tag{2.12}$$

Assuming small angles (which is appropriate because the airfoil is likely to stall once the local angle of attack or angle of sideslip exceeds 10 to 15 degrees), angle of attack and angle of sideslip can be written as

$$\alpha_i = \frac{w_i^i}{u_i^i} \tag{2.13}$$

$$\beta_i = \frac{v_i^i}{u_i^i} \tag{2.14}$$

The forces and moments for the individual section in its local coordinate frame are

$$F_{x,i}^i = \frac{1}{2}\rho(V_i^i)^2 S_i(C_{L,i}\sin\alpha_i \; - \; C_{D,i}\cos\alpha_i) \tag{2.15}$$

$$F_{y,i}^i = 0 \tag{2.16}$$

$$F_{z,i}^i = \frac{1}{2}\rho(V_i^i)^2 S_i(-C_{D,i}\sin\alpha_i \; - \; C_{L,i}\cos\alpha_i) \tag{2.17}$$

$$M_{x,i}^i = 0 \tag{2.18}$$

$$M^i_{y,i} = \frac{1}{2}\rho(V^i_i)^2 S_i c_i C_{M,i} \tag{2.19}$$

$$M^i_{z,i} = 0 \tag{2.20}$$

Again, using small angle approximations, Equations 2.15 - 2.20 can be simplified to

$$F^i_{x,i} = \frac{1}{2}\rho(V^i_i)^2 S_i (C_{L,i}\alpha_i \; - \; C_{D,i}) \tag{2.21}$$

$$F^i_{y,i} = 0 \tag{2.22}$$

$$F^i_{z,i} = \frac{1}{2}\rho(V^i_i)^2 S_i (-C_{D,i}\alpha_i \; - \; C_{L,i}) \tag{2.23}$$

$$M^i_{x,i} = 0 \tag{2.24}$$

$$M^i_{y,i} = \frac{1}{2}\rho(V^i_i)^2 S_i c_i C_{M,i} \tag{2.25}$$

$$M^i_{z,i} = 0 \tag{2.26}$$

where,

$$V^i_i = \sqrt{(u^i_i)^2 + (v^i_i)^2 + (w^i_i)^2} \tag{2.27}$$

Because different types of aerodynamic surfaces are modeled differently $C_{L,i}$, $C_{D,i}$, $C_{M,i}$, and α_i will differ depending on which surface type is used for that particular section (all-flying vs traditional). Details on the calculations of these parameters, as well as descriptions of the different control surface types, are discussed in Section 3.1.

2.3 Transformation of Forces to Global Coordinate Frame

Now that all of the force and moment equations have been determined in the local section coordinate frame they must be transformed to the aircraft body coordinate frame. This transformation allows all of the forces and moments from each section to be added together to obtain the general aircraft equations of motion. The transformation involves taking the inverse of the transformation matrix used to get the global velocities into the local frame. This is then multiplied by the force vector to get the force vector in the global frame. The same inverse transformation matrix is then multiplied by the moment vector in the local frame and added to the cross product of the section's position vector and the global force vector.

$$\mathbf{T}_{b/i} = \mathbf{T}_{i/b}^{-1} \tag{2.28}$$

$$\mathbf{F}_i^b = \mathbf{T}_{b/i} \begin{bmatrix} F_{x,i}^i \\ F_{y,i}^i \\ F_{z,i}^i \end{bmatrix} \tag{2.29}$$

$$\mathbf{M}_i^b = \mathbf{T}_{b/i} \begin{bmatrix} M_{x,i}^i \\ M_{y,i}^i \\ M_{z,i}^i \end{bmatrix} + \mathbf{r}_i^b \times \mathbf{F}_i^b \tag{2.30}$$

The resulting individual force and moment equations in the global coordinate frame for an arbitrary all-flying control surface with control deflection δ_i are,

$$F_{x,i}^b = -\frac{1}{2}\rho\, S_i\, (V_i^i)^2 \Big[\cos\theta_i \Big(C_{D_0,i} - \left(C_{L_0,i} + C_{L_\alpha,i}\,(\delta_i + \alpha_i)\right)(\delta_i + \alpha_i) \Big) + \sin\theta_i \Big(C_{L_0,i} + C_{L_\alpha,i}\,(\delta_i + \alpha_i) + C_{D_0,i}\,(\delta_i + \alpha_i) \Big) \Big] \tag{2.31}$$

$$F_{y,i}^b = \frac{1}{2}\rho\, S_i\, (V_i^i)^2 \sin\phi_i \Big[-\sin\theta_i \Big(C_{D_0,i} - \left(C_{L_0,i} + C_{L_\alpha,i}\,(\delta_i + \alpha_i)\right)(\delta_i + \alpha_i) \Big) + \cos\theta_i \Big(C_{L_0,i} + C_{L_\alpha,i}\,(\delta_i + \alpha_i) + C_{D_0,i}\,(\delta_i + \alpha_i) \Big) \Big] \tag{2.32}$$

$$F^b_{z,i} = \frac{1}{2}\rho\, S_i\, (V^i_i)^2 \cos\phi_i \Big[\sin\theta_i \Big(C_{D_0,i} \,-\, (C_{L_0,i} \,+\, C_{L_\alpha,i}\,(\delta_i \,+\, \alpha_i))\,(\delta_i \,+\, \alpha_i) \Big) \\ -\, \cos\theta_i \Big(C_{L_0,i} \,+\, C_{L_\alpha,i}\,(\delta_i \,+\, \alpha_i) \,+\, C_{D_0,i}\,(\delta_i \,+\, \alpha_i) \Big) \Big] \quad (2.33)$$

$$M^b_{x,i} = r_{y,i}\, F^b_{z,i} \,-\, r_{z,i}\, F^b_{y,i} \quad (2.34)$$

$$M^b_{y,i} = -r_{x,i}\, F^b_{z,i} \,+\, r_{z,i}\, F^b_{x,i} \,+\, \frac{1}{2}\rho\, S_i\, c_i\, (V^i_i)^2\, C_{M_0,i} \cos\phi_i \quad (2.35)$$

$$M^b_{z,i} = r_{x,i}\, F^b_{y,i} \,-\, r_{y,i}\, F^b_{x,i} \,+\, \frac{1}{2}\rho\, S_i\, c_i\, (V^i_i)^2\, C_{M_0,i} \sin\phi_i \quad (2.36)$$

And for a segment with a traditional control surface with deflection δ_i,

$$F^b_{x,i} = -\frac{1}{2}\rho\, S_i\, (V^i_i)^2 \Big[\cos\theta_i \Big(C_{D_0,i} \,-\, (C_{L_0,i} \,+\, C_{L_\delta,i}\delta_i \,+\, C_{L_\alpha,i}\alpha_i)\,\alpha_i \Big) \\ +\, \sin\theta_i \Big(C_{L_0,i} \,+\, C_{L_\delta,i}\delta_i \,+\, C_{L_\alpha,i}\alpha_i \,+\, C_{D_0,i}\alpha_i \Big) \Big] \quad (2.37)$$

$$F^b_{y,i} = \frac{1}{2}\rho\, S_i\, (V^i_i)^2 \sin\phi_i \Big[-\sin\theta_i \Big(C_{D_0,i} \,-\, (C_{L_0,i} \,+\, C_{L_\delta,i}\delta_i \,+\, C_{L_\alpha,i}\alpha_i)\,\alpha_i \Big) \\ +\, \cos\theta_i \Big(C_{L_0,i} \,+\, C_{L_\delta,i}\delta_i \,+\, C_{L_\alpha,i}\alpha_i \,+\, C_{D_0,i}\alpha_i \Big) \Big] \quad (2.38)$$

$$F^b_{z,i} = \frac{1}{2}\rho\, S_i\, (V^i_i)^2 \cos\phi_i \Big[\sin\theta_i \Big(C_{D_0,i} \,-\, (C_{L_0,i} \,+\, C_{L_\delta,i}\delta_i \,+\, C_{L_\alpha,i}\alpha_i)\,\alpha_i \Big) \\ -\, \cos\theta_i \Big(C_{L_0,i} \,+\, C_{L_\delta,i}\delta_i \,+\, C_{L_\alpha,i}\alpha_i \,+\, C_{D_0,i}\alpha_i \Big) \Big] \quad (2.39)$$

$$M^b_{x,i} = r_{y,i}\, F^b_{z,i} \,-\, r_{z,i}\, F^b_{y,i} \quad (2.40)$$

$$M^b_{y,i} = -r_{x,i}\, F^b_{z,i} \,+\, r_{z,i}\, F^b_{x,i} \,+\, \frac{1}{2}\rho\, S_i\, c_i\, (V^i_i)^2\, (C_{M_0,i} \,+\, C_{M_\delta,i}\delta_i) \cos\phi_i \tag{2.41}$$

$$M^b_{z,i} = r_{x,i}\, F^b_{y,i} \,-\, r_{y,i}\, F^b_{x,i} \,+\, \frac{1}{2}\rho\, S_i\, c_i\, (V^i_i)^2\, (C_{M_0,i} \,+\, C_{M_\delta,i}\delta_i) \sin\phi_i \tag{2.42}$$

Each section's velocity components are

$$\begin{aligned} u^i_i = \cos\theta_i(u^b_b \,+\, Q\, r_{z,i} \,-\, R\, r_{y,i}) \,-\, \cos\phi_i \sin\theta_i(w^b_b \,+\, P\, r_{y,i} \,-\, Q\, r_{x,i}) \\ +\, \sin\phi_i \sin\theta_i(v^b_b \,-\, P\, r_{z,i} \,+\, R\, r_{x,i}) \end{aligned} \tag{2.43}$$

$$v^i_i = \cos\phi_i(v^b_b \,-\, P\, r_{z,i} \,+\, R\, r_{x,i}) \,+\, \sin\phi_i(w^b_b \,+\, P\, r_{y,i} \,-\, Q\, r_{x,i}) \tag{2.44}$$

$$\begin{aligned} w^i_i = \sin\theta_i(u^b_b \,+\, Q\, r_{z,i} \,-\, R\, r_{y,i}) \,+\, \cos\phi_i \cos\theta_i(w^b_b \,+\, P\, r_{y,i} \,-\, Q\, r_{x,i}) \\ -\, \sin\phi_i \cos\theta_i(v^b_b \,-\, P\, r_{z,i} \,+\, R\, r_{x,i}) \end{aligned} \tag{2.45}$$

Now that the force and moment equations of an arbitrary section, with respect to the aircraft body frame, have been defined, the next step is to assemble all of the components into the total force and moment equations for the entire aircraft.

Chapter 3

Linearized Aerodynamic Model

The mathematical model used to characterize the behavior of the aircraft involves setting up the force and moment equations to be of the form $\mathbf{f} = \mathbf{Dx} + \mathbf{U}\boldsymbol{\delta}$, where $\mathbf{f}$ is a vector containing the aerodynamic forces and moments, $\mathbf{D}$ is the stability derivative matrix, the state vector $\mathbf{x}$ contains the linear and angular velocity components of the aircraft, $\mathbf{U}$ is the control derivative matrix, and the control vector $\boldsymbol{\delta}$ consists of the control surface deflection angles.

$$\mathbf{f} = \begin{bmatrix} X \\ Y \\ Z \\ L \\ M \\ N \end{bmatrix} \tag{3.1}$$

$$\mathbf{x} = \begin{bmatrix} u \\ v \\ w \\ P \\ Q \\ R \end{bmatrix} \tag{3.2}$$

$$\boldsymbol{\delta} = \begin{bmatrix} \delta_e & \delta_a & \delta_r \end{bmatrix}^T \tag{3.3}$$

In order to use a model of this form, the equations must be linear in order to

have **D** and **U** be constant matrices. The first step to obtaining these linear EoMs is to develop a set of equations for the aerodynamic coefficients in terms of the state and control vector variables. Once a complete set of equations is formed that depend only on the state and control variables they can be linearized. The linearization method, based on small disturbance theory (discussed in Section 1.5.2), takes a function($f(x, y, z, \ldots)$) and determines an equation for the Δ of the function's value from the initial set-point point condition $f_0 = f(\mathbf{x_0})$, where $\mathbf{x_0} = [x_0, y_0, z_0, \ldots]$ is the value of the state vector at the initial set-point. The method involves taking the partial derivative of the function with respect to each state variable, evaluating that derivative at the initial set-point and then multiplying it by the disturbance value of its respective state variable. All of these components are then summed to yield the final form

$$\Delta f \approx \frac{\partial f}{\partial x}\Big|_{\mathbf{x_0}} \delta x \; + \; \frac{\partial f}{\partial y}\Big|_{\mathbf{x_0}} \delta y \; + \; \frac{\partial f}{\partial z}\Big|_{\mathbf{x_0}} \delta z + \ldots \tag{3.4}$$

3.1 Aerodynamic Coefficients

Equations for the aerodynamic coefficients of an individual section will vary depending on the section's airfoil shape as well as what, if any, control surface type it contains. Prior to using the strip model the viscous panel code Xfoil[8] is used to obtain lift, drag, and moment coefficient data for each airfoil used. From these data a set of linear equations is formed to calculate the value of the coefficients that are dependent only upon state and control variables. Two types of control surfaces are used with this model, an 'all-flying' control surface in which the whole section acts as the control surface, and a traditional control surface where the section has a movable flap with a hinge at some location aft of the leading edge.

3.1.1 Total Coefficient Equations

Since the two control surface types have different methods of control surface deflection their aerodynamic properties are calculated differently.

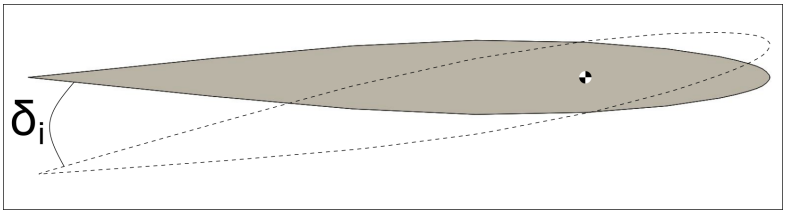

Figure 3.1: All-Flying Control Surface

An all-flying control surface(Figure 3.1) is a section in which the entire surface rotates when a control surface deflection is commanded. This makes the calculations for the airfoil simpler since the aerodynamic properties of the airfoil do not change with control surface deflection. The control surface deflection is merely added to the current section angle of attack to get a new effective angle of attack of the section. the effective angle of attack is given by

$$\alpha_{eff} = \alpha_i + \delta_i \tag{3.5}$$

where δ_i is the control surface deflection for the segment. The aerodynamic coefficient equations for this type of section are

$$C_{L,i} = C_{L_0,i} + C_{L_\alpha,i}\,\alpha_{eff} \tag{3.6}$$

$$C_{D,i} = C_{D_0,i} \tag{3.7}$$

$$C_{M,i} = C_{M_0,i} \tag{3.8}$$

The assumption of a constant section drag coefficient means that this approach cannot be used for performance calculations. However since the goal of this method is to create an approximation for use in designing a controller, this simplifying assumption was deemed appropriate.

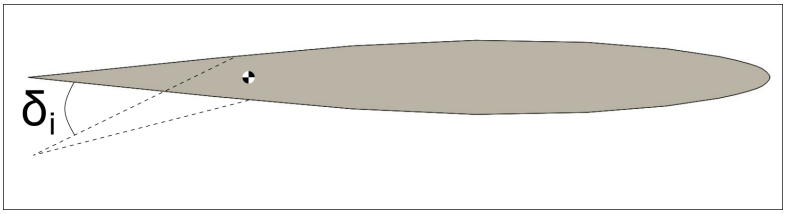

Figure 3.2: Traditional Control Surface

A traditional control surface(Figure 3.2) is one that has a flap with a hinge located some percentage aft of the airfoil leading edge. This means that changing the control surface deflection effectively changes the camber-line of the airfoil changing its aerodynamic properties. The aerodynamic coefficient equations for this control surface type are

$$C_{L,i} = C_{L_0,i} + C_{L_\alpha,i}\,\alpha_i + C_{L_\delta,i}\,\delta_i \tag{3.9}$$

$$C_{D,i} = C_{D_0,i} \tag{3.10}$$

$$C_{M,i} = C_{M_0,i} + C_{M_\delta,i}\,\delta_i \tag{3.11}$$

Where $C_{L_\delta,i}$ is the derivative of ΔC_L with respect to δ, and $C_{M_\delta,i}$ is the derivative of ΔC_M with respect to δ, the calculation of these values is explained in detail in 3.1.2.

3.1.2 Linearized Airfoil Data

Due to the small relative angles of attack each individual airfoil section will experience, it is possible to characterize the lift, drag, and moment coefficients of each section as a linear function of angle of attack and control surface deflection. If a more accurate model is needed or the airfoil behaves in a non-linear fashion it is possible to redo the analysis with either a symbolic equation in terms of α and δ_i, or a lookup table and numerical derivation.

The method for determining the linear equations involved running Xfoil for each airfoil profile over a range of α's at an assumed operating Reynolds number. A linear data fit was used to get the characterizing equation for each coefficient. For the example aircraft used to develop this model, two different airfoils were used.

The PSU-94-097 airfoil was used for all main wing sections, while the NACA-63A010 symmetric airfoil was used for all tail sections. Any airfoil can be used within a model provided that the surface profile is known and can be input into Xfoil.

For the main wing an assumed operating Reynolds number of 400,000 was used. This corresponds to a wing with a chord of .4064 m traveling at 15 m/s at standard sea-level. Xfoil was run for α's ranging from -10° to 10°. The lift, drag, and moment coefficient vs α plots are shown in Figures 3.3a, 3.3b, and 3.3d respectively.

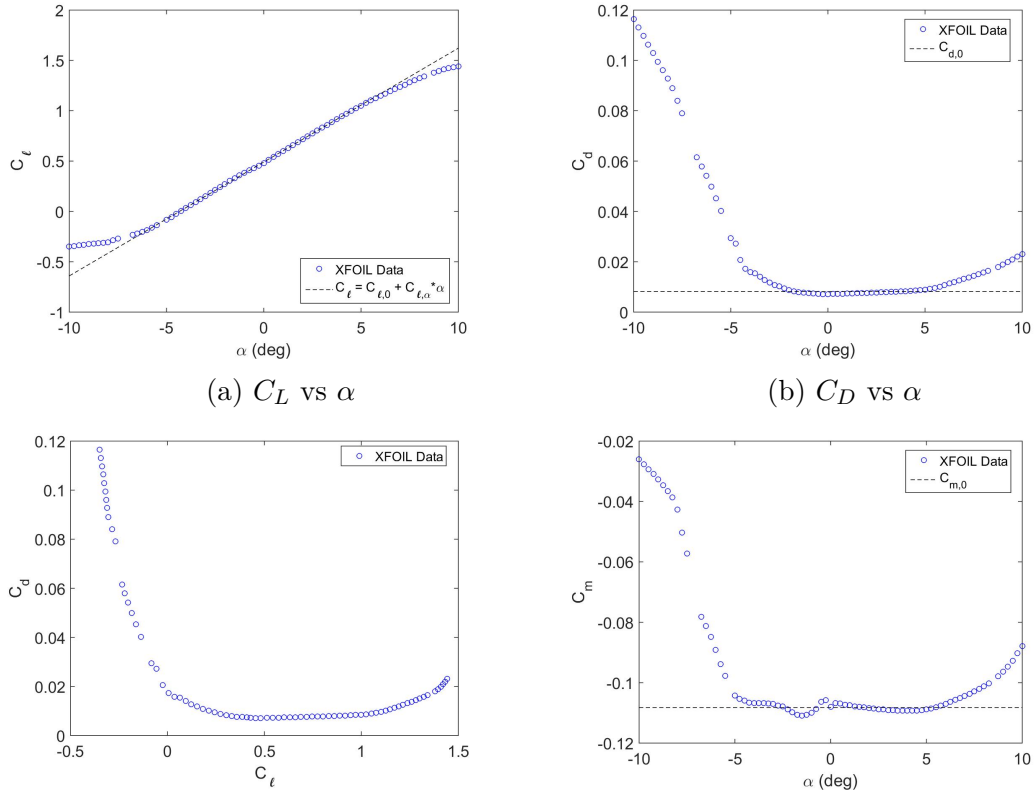

(a) C_L vs α

(b) C_D vs α

(c) C_L vs C_D

(d) C_M vs α

Figure 3.3: PSU-94-097 Airfoil

Since this model focuses on linearizing about a trimmed cruise condition the expected effective angle of attack on any given surface should be small. This allows the drag and moment coefficients to approximated as constant, with their respective values being equal to the average of the values for $\alpha = -5°$ to 5°. The value of the lift coefficient at $\alpha = 0$ was taken to be C_{L_0} and the slope of the data fit from $\alpha = -5°$ to 5° to be C_{L_α}. The resulting aerodynamic coefficients for the PSU-94-097

airfoil are given in Table 3.1.

PSU-94-097	
C_{L_0}	0.4904
C_{L_α}(per deg)	0.1131
C_{D_0}	0.00815
C_{M_0}	-0.1083

Table 3.1: Aerodynamic Coefficients for PSU-94-097 Airfoil

For the tails an assumed operating Reynolds number of 125,000 was used. This corresponds to a wing with a chord of .127 m traveling at 15 m/s at standard sea-level. Xfoil was run for α's ranging from -10° to 10°, however the cases above 7.5° and below $-7.5°$ failed to converge. The lift, drag, and moment coefficient vs α plots are shown in Figures 3.4a, 3.4b, and 3.4d respectively.

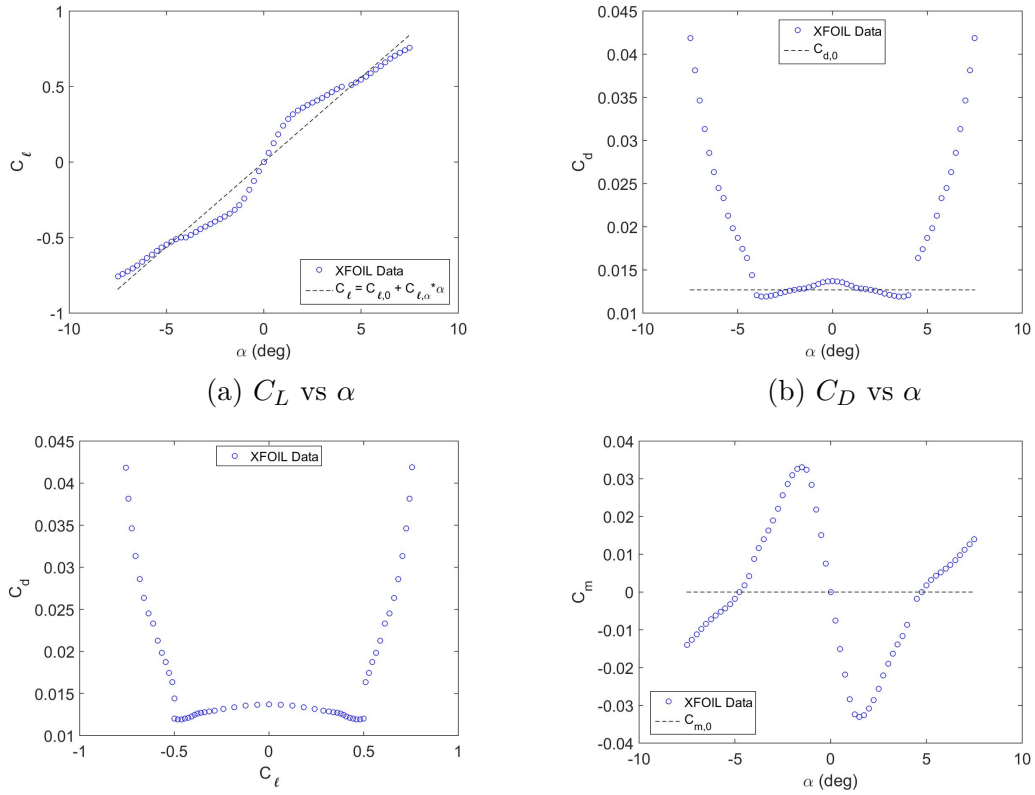

(a) C_L vs α (b) C_D vs α

(c) C_L vs C_D (d) C_M vs α

Figure 3.4: NACA-63A010 Airfoil

Similar to the PSU airfoil, C_{D_0} is assumed to be constant and equal to the average value over the α range of $-4°$ to $4°$, The bounds for the average are determined by finding the area on the plot that is approximately constant. Since the airfoil is symmetric the moment coefficient behaves symmetrically and averages to 0. This is deemed acceptable since the change in the moment coefficient is small. In addition from Thin Airfoil Theory the moment coefficient about the $\frac{1}{4}$ chord point is 0 for a symmetric airfoil, so the assumption has some basis in theory. Since it is a symmetric airfoil $C_{L_0} = 0$ and C_{L_α} is obtained from the slope of the C_L vs α curve. The resulting aerodynamic coefficients for the NACA-63A010 airfoil are given in Table 3.2.

NACA-63A010	
C_{L_0}	0.00
C_{L_α}(per deg)	0.1122
C_{D_0}	0.01268
C_{M_0}	0.00

Table 3.2: Aerodynamic Coefficients for NACA-63A010 Airfoil

The method for determining the effects of control surface deflection involved running Xfoil for the airfoil profile that would use a traditional flap style control surface. The Xfoil runs were done using the same assumed operating Reynolds number as for the regular coefficients, using an α sweep for varying flap deflections. For the control surface modifier calculations the NACA-63A010 airfoil was used with a hinge location of 70% chord aft of the leading edge. The Reynolds number used was the same as for the airfoil with no flap. The airfoil was analyzed in Xfoil with flap deflections of -10°, -5°, 0°, 5°, and 10°, Xfoil's convention had a positive deflection downward. For each flap deflection a sweep of α's was performed until Xfoil no longer converged. The lift, drag, and moment coefficient vs α plots can be seen in Figures 3.5a, 3.5b, and 3.5d respectively.

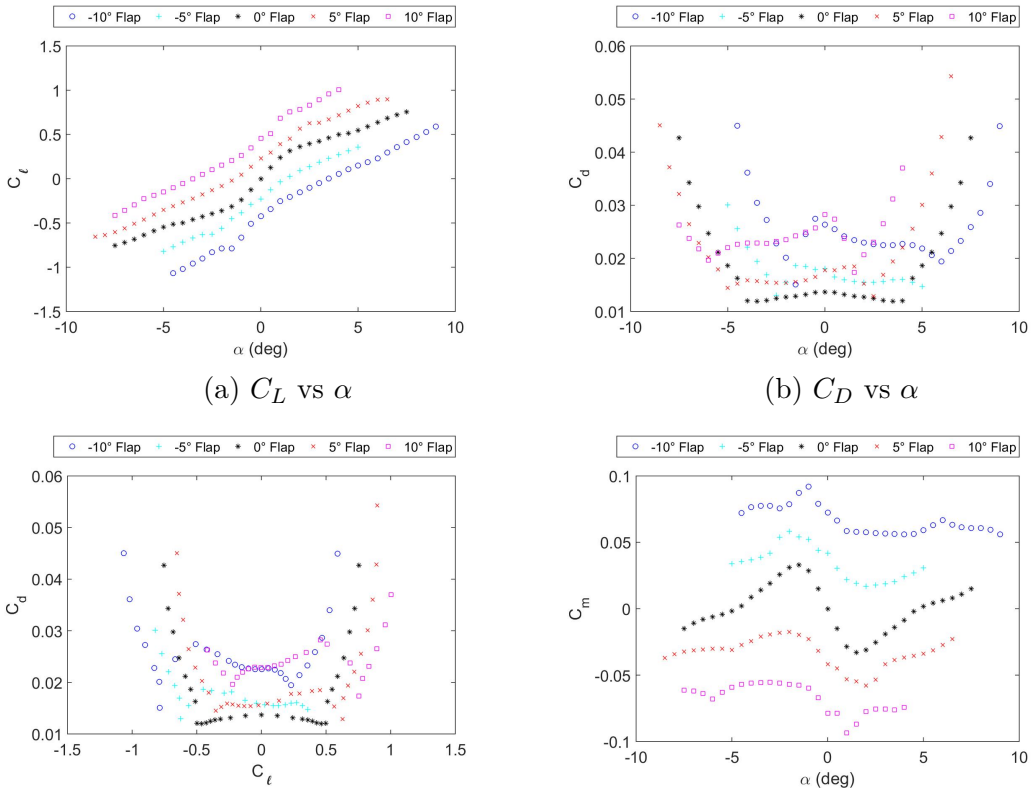

(a) C_L vs α

(b) C_D vs α

(c) C_L vs C_D

(d) C_M vs α

Figure 3.5: NACA-63A010 with various flap deflection angles

As seen in Figure 3.5a the lift curve is shifted up for increasing flap angles, and shifted down for decreasing angles. This means that the lift coefficient increases/decreases linearly with control surface deflection. To calculate this relationship the difference between the lift coefficient at a given flap deflection and 0 flap deflection was taken and then plotted vs flap deflection angle. This was done for a variety of α's to ensure the linear relationship was not dependent upon α. As shown in Figure 3.6a the relationship is indeed linear and not heavily dependent on α. The average of all of the slopes becomes C_{L_δ} which for this airfoil is 0.04668(per degree).

Figure 3.5b shows that for small angles of attack C_D remains relatively constant except for high control surface deflection angles. Since the drag is relatively low this is seen as negligible.

Figure 3.5d shows a similar relationship as the lift albeit a negative linear relationship rather than a positive one. Since the average value of C_M is 0, only the average values for each deflection angle need to be plotted. As shown in Figure

3.6b the relationship is inversely linear, the slope of this line becomes C_{M_δ} which for this airfoil is -0.0069(per degree).

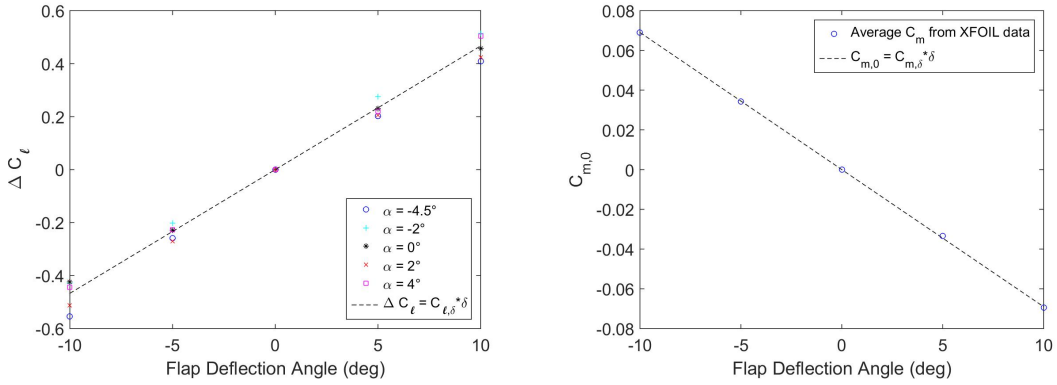

(a) ΔC_L vs δ for various α's (b) Avg C_M vs δ

Figure 3.6: NACA-63A010 with Control Surface Deflections

It is important to note that these calculations are done assuming trailing edge down is a positive control surface deflection, depending on the application for the specific section that may not be the case depending on how a specific section's local coordinate frame is defined as well as what type of control surface it has (aileron, elevator, or rudder).

3.1.3 Corrections for 3D Aerodynamic Effects

Since the aerodynamic coefficients calculated in Section 3.1.2 are determined using 2D Xfoil data, modifications are necessary to better approximate for the losses on a 3D surface due to downwash and tip effects. The effect of downwash was applied to every surface in the form of a modifier to the lift curve slope (C_{L_α}) of the section airfoil. This modifier, derived from lifting line theory (as discussed in Section 1.5.1), is $a = \frac{a_0}{1+\frac{a_0}{\pi\, AR\, e}}$ [3, p. 443], where a is the modified lift curve slope, a_0 is the 2D lift curve slope obtained from Xfoil, AR is the aspect ratio, and e is the span efficiency factor. The aspect ratio ($\frac{b^2}{S}$) is that of the entire contiguous lifting surface that the section is a part of, for instance when doing the calculation for a section of the main wing the aspect ratio for the entire wing is used.

Tip effects are modeled by approximating the lift distribution of the wing as trapezoidal. This trapezoidal lift distribution enforces the condition of zero lift

at the wingtips and approximates the lift for the outboard sections as linear. To do this the main wing calculations are done separately from those for the rest of the aerodynamic surfaces. Then for the outboard sections of the wing C_{L_0} as well as the already modified C_{L_α} are divided by 2. This gives a value for the lift on these sections as being the average of the lift on the inboard side of the section (full lift) and the lift at the wingtip (zero). This approximation works well enough for this application while maintaining simplicity of the model. If future applications find that this approximation is no longer adequate an elliptic distribution modifier could be added across the whole wing surface.

3.2 Linearization of Section EoMs

The linearization for this application is done about a desired steady state flight condition. This flight condition is a steady, wings-level, constant altitude, constant lift cruise condition. In essence a fixed forward velocity and angle of attack, as well as a fixed elevator deflection required to maintain equilibrium, all other states/controls are zero. The set-point state and control vectors are

$$\mathbf{x_0} = \begin{bmatrix} u_0 \\ v_0 \\ w_0 \\ P_0 \\ Q_0 \\ R_0 \end{bmatrix} = \begin{bmatrix} u_0 \\ 0 \\ w_0 \\ 0 \\ 0 \\ 0 \end{bmatrix} \tag{3.12}$$

$$\boldsymbol{\delta_0} = \begin{bmatrix} \delta_{e,0} & \delta_{a,0} & \delta_{r,0} \end{bmatrix}^T = \begin{bmatrix} \delta_{e,0} & 0 & 0 \end{bmatrix}^T \tag{3.13}$$

where, u_0 and w_0 are determined from the aircraft's forward velocity and angle of attack. The relationships are, $u_0 = V\cos\alpha$ and $w_0 = V\sin\alpha$. The aircraft's trimmed Euler angles can be derived using the assumption of wings-level, constant altitude flight. ϕ_0^E is zero from the wings-level assumption, ψ_0^E is arbitrarily defined and for simplification is set to zero, and θ_0^E is equal to α due to the flight path angle being zero through the constant altitude assumption.

The linearized force and moment equations for an individual section are

$$\Delta F_{x,i} = \left.\frac{\partial F_{x,i}}{\partial u}\right|_{\mathbf{x_0}} \delta u \;+\; \left.\frac{\partial F_{x,i}}{\partial v}\right|_{\mathbf{x_0}} \delta v \;+\; \left.\frac{\partial F_{x,i}}{\partial w}\right|_{\mathbf{x_0}} \delta w \;+\; \left.\frac{\partial F_{x,i}}{\partial P}\right|_{\mathbf{x_0}} \delta P + \left.\frac{\partial F_{x,i}}{\partial Q}\right|_{\mathbf{x_0}} \delta Q \;+\; \left.\frac{\partial F_{x,i}}{\partial R}\right|_{\mathbf{x_0}} \delta R \;+\; \left.\frac{\partial F_{x,i}}{\partial \delta_i}\right|_{\boldsymbol{\delta_0}} \delta\delta_i \quad (3.14)$$

$$\Delta F_{y,i} = \left.\frac{\partial F_{y,i}}{\partial u}\right|_{\mathbf{x_0}} \delta u \;+\; \left.\frac{\partial F_{y,i}}{\partial v}\right|_{\mathbf{x_0}} \delta v \;+\; \left.\frac{\partial F_{y,i}}{\partial w}\right|_{\mathbf{x_0}} \delta w \;+\; \left.\frac{\partial F_{y,i}}{\partial P}\right|_{\mathbf{x_0}} \delta P + \left.\frac{\partial F_{y,i}}{\partial Q}\right|_{\mathbf{x_0}} \delta Q \;+\; \left.\frac{\partial F_{y,i}}{\partial R}\right|_{\mathbf{x_0}} \delta R \;+\; \left.\frac{\partial F_{y,i}}{\partial \delta_i}\right|_{\boldsymbol{\delta_0}} \delta\delta_i \quad (3.15)$$

$$\Delta F_{z,i} = \left.\frac{\partial F_{z,i}}{\partial u}\right|_{\mathbf{x_0}} \delta u \;+\; \left.\frac{\partial F_{z,i}}{\partial v}\right|_{\mathbf{x_0}} \delta v \;+\; \left.\frac{\partial F_{z,i}}{\partial w}\right|_{\mathbf{x_0}} \delta w \;+\; \left.\frac{\partial F_{z,i}}{\partial P}\right|_{\mathbf{x_0}} \delta P + \left.\frac{\partial F_{z,i}}{\partial Q}\right|_{\mathbf{x_0}} \delta Q \;+\; \left.\frac{\partial F_{z,i}}{\partial R}\right|_{\mathbf{x_0}} \delta R \;+\; \left.\frac{\partial F_{z,i}}{\partial \delta_i}\right|_{\boldsymbol{\delta_0}} \delta\delta_i \quad (3.16)$$

$$\Delta M_{x,i} = \left.\frac{\partial M_{x,i}}{\partial u}\right|_{\mathbf{x_0}} \delta u \;+\; \left.\frac{\partial M_{x,i}}{\partial v}\right|_{\mathbf{x_0}} \delta v \;+\; \left.\frac{\partial M_{x,i}}{\partial w}\right|_{\mathbf{x_0}} \delta w \;+\; \left.\frac{\partial M_{x,i}}{\partial P}\right|_{\mathbf{x_0}} \delta P + \left.\frac{\partial M_{x,i}}{\partial Q}\right|_{\mathbf{x_0}} \delta Q \;+\; \left.\frac{\partial M_{x,i}}{\partial R}\right|_{\mathbf{x_0}} \delta R \;+\; \left.\frac{\partial M_{x,i}}{\partial \delta_i}\right|_{\boldsymbol{\delta_0}} \delta\delta_i \quad (3.17)$$

$$\Delta M_{y,i} = \left.\frac{\partial M_{y,i}}{\partial u}\right|_{\mathbf{x_0}} \delta u \;+\; \left.\frac{\partial M_{y,i}}{\partial v}\right|_{\mathbf{x_0}} \delta v \;+\; \left.\frac{\partial M_{y,i}}{\partial w}\right|_{\mathbf{x_0}} \delta w \;+\; \left.\frac{\partial M_{y,i}}{\partial P}\right|_{\mathbf{x_0}} \delta P + \left.\frac{\partial M_{y,i}}{\partial Q}\right|_{\mathbf{x_0}} \delta Q \;+\; \left.\frac{\partial M_{y,i}}{\partial R}\right|_{\mathbf{x_0}} \delta R \;+\; \left.\frac{\partial M_{y,i}}{\partial \delta_i}\right|_{\boldsymbol{\delta_0}} \delta\delta_i \quad (3.18)$$

$$\Delta M_{z,i} = \left.\frac{\partial M_{z,i}}{\partial u}\right|_{\mathbf{x_0}} \delta u \;+\; \left.\frac{\partial M_{z,i}}{\partial v}\right|_{\mathbf{x_0}} \delta v \;+\; \left.\frac{\partial M_{z,i}}{\partial w}\right|_{\mathbf{x_0}} \delta w \;+\; \left.\frac{\partial M_{z,i}}{\partial P}\right|_{\mathbf{x_0}} \delta P + \left.\frac{\partial M_{z,i}}{\partial Q}\right|_{\mathbf{x_0}} \delta Q \;+\; \left.\frac{\partial M_{z,i}}{\partial R}\right|_{\mathbf{x_0}} \delta R \;+\; \left.\frac{\partial M_{z,i}}{\partial \delta_i}\right|_{\boldsymbol{\delta_0}} \delta\delta_i \quad (3.19)$$

These linearized equations for a single section can be put into the same matrix form as described in the beginning of the chapter.

$$\begin{bmatrix} \Delta F_{x,i} \\ \Delta F_{y,i} \\ \Delta F_{z,i} \\ \Delta M_{x,i} \\ \Delta M_{y,i} \\ \Delta M_{z,i} \end{bmatrix} = \mathbf{D_i} \begin{bmatrix} \delta u \\ \delta v \\ \delta w \\ \delta P \\ \delta Q \\ \delta R \end{bmatrix} + \mathbf{U_i}\, \delta\delta_i \tag{3.20}$$

where,

$$\mathbf{D_i} = \begin{bmatrix} \frac{\partial F_{x,i}}{\partial u} & \frac{\partial F_{x,i}}{\partial v} & \frac{\partial F_{x,i}}{\partial w} & \frac{\partial F_{x,i}}{\partial P} & \frac{\partial F_{x,i}}{\partial Q} & \frac{\partial F_{x,i}}{\partial R} \\ \frac{\partial F_{y,i}}{\partial u} & \frac{\partial F_{y,i}}{\partial v} & \frac{\partial F_{y,i}}{\partial w} & \frac{\partial F_{y,i}}{\partial P} & \frac{\partial F_{y,i}}{\partial Q} & \frac{\partial F_{y,i}}{\partial R} \\ \frac{\partial F_{z,i}}{\partial u} & \frac{\partial F_{z,i}}{\partial v} & \frac{\partial F_{z,i}}{\partial w} & \frac{\partial F_{z,i}}{\partial P} & \frac{\partial F_{z,i}}{\partial Q} & \frac{\partial F_{z,i}}{\partial R} \\ \frac{\partial M_{x,i}}{\partial u} & \frac{\partial M_{x,i}}{\partial v} & \frac{\partial M_{x,i}}{\partial w} & \frac{\partial M_{x,i}}{\partial P} & \frac{\partial M_{x,i}}{\partial Q} & \frac{\partial M_{x,i}}{\partial R} \\ \frac{\partial M_{y,i}}{\partial u} & \frac{\partial M_{y,i}}{\partial v} & \frac{\partial M_{y,i}}{\partial w} & \frac{\partial M_{y,i}}{\partial P} & \frac{\partial M_{y,i}}{\partial Q} & \frac{\partial M_{y,i}}{\partial R} \\ \frac{\partial M_{z,i}}{\partial u} & \frac{\partial M_{z,i}}{\partial v} & \frac{\partial M_{z,i}}{\partial w} & \frac{\partial M_{z,i}}{\partial P} & \frac{\partial M_{z,i}}{\partial Q} & \frac{\partial M_{z,i}}{\partial R} \end{bmatrix} \tag{3.21}$$

and,

$$\mathbf{U_i} = \begin{bmatrix} \frac{\partial F_{x,i}}{\partial \delta_i} \\ \frac{\partial F_{y,i}}{\partial \delta_i} \\ \frac{\partial F_{z,i}}{\partial \delta_i} \\ \frac{\partial M_{x,i}}{\partial \delta_i} \\ \frac{\partial M_{y,i}}{\partial \delta_i} \\ \frac{\partial M_{z,i}}{\partial \delta_i} \end{bmatrix} \tag{3.22}$$

The equations of the individual elements of the **D** and **U** matrices for an arbitrary section can be found in Appendix A with the elements for an all-flying control surface found in A.1 and those for a traditional control surface in A.2. The equations in the appendix come from completing the partial derivatives of the equations developed in Chapter 2 and then substituting in the set-point conditions. This yields equations entirely in terms of known variables for each section. The **D** and **U** matrices for a given segment can then easily be calculated by plugging in the geometry, location, and orientation information for that particular section as well as the global environmental variables and set-point conditions.

3.3 Stability and Control Derivatives

The key advantage to having the force and moment equations in the linear form $\Delta\mathbf{f} = \mathbf{D}\delta\mathbf{x} + \mathbf{U}\delta\boldsymbol{\delta}$ is that it enables the creation of the linear equations of motion of the aircraft. These linear equations of motion are often expressed in terms of the 'stability and control derivatives' of the aircraft. In addition to their use in the modeling of the aircraft's dynamics, a few key stability and control derivatives give insight into the stability and controllability of the aircraft just from the sign and magnitude of their values. This allows determining the viability of a design without the need to actually simulate the aircraft's response. In order to calculate these stability and control derivatives, first the section $\mathbf{D_i}$ and $\mathbf{U_i}$ matrices must be combined to get a global aircraft $\mathbf{D}$ and $\mathbf{U}$ matrix. The columns of the $\mathbf{U}$ matrix must then be combined with the columns of like control surface types (i.e. aileron, elevator, or rudder). The components of the $\mathbf{D}$ and $\mathbf{U}$ matrices are then used to calculate the dimensional stability and control derivatives. These dimensional derivatives are then nondimensionalized to produce standardized values that can be compared to the output of vortex lattice codes as well as be used to determine aircraft static stability and control.

3.3.1 Assembly of Section Equations of Motion

Once the $\mathbf{D_i}$ and $\mathbf{U_i}$ matrices for each individual section are calculated, they can be summed to get the $\mathbf{D}$ and $\mathbf{U}$ matrices of the global aircraft.

$$\begin{bmatrix} \Delta X^b \\ \Delta Y^b \\ \Delta Z^b \\ \Delta L^b \\ \Delta M^b \\ \Delta N^b \end{bmatrix} = \sum \mathbf{D_i} \begin{bmatrix} \delta u \\ \delta v \\ \delta w \\ \delta P \\ \delta Q \\ \delta R \end{bmatrix} + \begin{bmatrix} \mathbf{U_1} & \mathbf{U_2} & \cdots & \mathbf{U_n} \end{bmatrix} \begin{bmatrix} \delta_1 \\ \delta_2 \\ \vdots \\ \delta_n \end{bmatrix} \tag{3.23}$$

where n is the number of sections with control surfaces. The $\mathbf{U_i}$ matrices are appended to one another rather than summing their individual elements in order to be able to organize them by control surface type. The $\mathbf{U}$ matrix columns for sections that contain the same type of control surface are combined so that the

final equations take the form

$$\begin{bmatrix} \Delta X^b \\ \Delta Y^b \\ \Delta Z^b \\ \Delta L^b \\ \Delta M^b \\ \Delta N^b \end{bmatrix} = \sum \mathbf{D_i} \begin{bmatrix} \delta u \\ \delta v \\ \delta w \\ \delta P \\ \delta Q \\ \delta R \end{bmatrix} + \begin{bmatrix} \mathbf{U_e} & \mathbf{U_a} & \mathbf{U_r} \end{bmatrix} \begin{bmatrix} \delta_e \\ \delta_a \\ \delta_r \end{bmatrix} \tag{3.24}$$

If a section acts as more than one control surface (e.g. elevon, ruddervator, etc.) then the column for that section can be split into longitudinal and lateral parts. The longitudinal elements (F_x, F_z, and M_y) are added to the elevator column. While the lateral elements (F_y, M_x, and M_z) are added to either the aileron or rudder column depending on what is appropriate for that control surface. This split assumes that the longitudinal/lateral coupling of the aircraft is negligible, which for most conventional aircraft configurations is a valid assumption.

3.3.2 Linear Equations of Motion and Nondimensional Derivatives

The components of the global **D** and **U** matrices are the dimensional stability and control derivatives of the entire aircraft. These dimensional derivatives are used to form linear equations for the aerodynamic forces and moments as functions of the disturbance state and control variables. Assuming the longitudinal and lateral coupling derivatives are negligible, the final linear force and moment equations are

$$\Delta X = X_u \delta u + X_w \delta w + X_Q \delta Q + X_{\delta_e} \delta \delta_e \tag{3.25}$$

$$\Delta Y = Y_v \delta v + Y_P \delta P + Y_R \delta R + Y_{\delta_a} \delta \delta_a + Y_{\delta_r} \delta \delta_r \tag{3.26}$$

$$\Delta Z = Z_u \delta u + Z_w \delta w + Z_Q \delta Q + Z_{\delta_e} \delta \delta_e \tag{3.27}$$

$$\Delta L = L_v \delta v + L_P \delta P + L_R \delta R + L_{\delta_a} \delta \delta_a + L_{\delta_r} \delta \delta_r \tag{3.28}$$

$$\Delta M = M_u \delta u + M_w \delta w + M_Q \delta Q + M_{\delta_e} \delta \delta_e \tag{3.29}$$

$$\Delta N = N_v \delta v + N_P \delta P + N_R \delta R + N_{\delta_a} \delta \delta_a + N_{\delta_r} \delta \delta_r \tag{3.30}$$

The capital letters with the subscripts represent the dimensional derivatives, with the capital letter representing the force/moment and the subscript representing the variable the derivative was taken with respect to.

Now that we have linear equations for the aerodynamic forces and moments we return to the generalized equations of motion for an aircraft given by Equations 2.2 - 2.7 from Section 2.1. Plugging in the Δ force and moment equations in terms of the stability and control derivatives and the disturbance inputs, as well as eliminating the steady-state reference forces and moments, results in linear equations of motion for disturbance linear and angular accelerations of the aircraft.

$$\delta\dot{u} = \frac{\Delta X}{m} - g\Delta\theta\cos\theta_0 - w_0\delta Q \tag{3.31}$$

$$\delta\dot{v} = \frac{\Delta Y}{m} + g\Delta\phi\cos\theta_0 - u_0\delta R + w_0\delta P \tag{3.32}$$

$$\delta\dot{w} = \frac{\Delta Z}{m} - g\Delta\theta\sin\theta_0 + u_0\delta Q \tag{3.33}$$

$$\delta\dot{P} = \frac{\Delta L}{I_x} \tag{3.34}$$

$$\delta\dot{Q} = \frac{\Delta M}{I_y} \tag{3.35}$$

$$\delta\dot{R} = \frac{\Delta N}{I_z} \tag{3.36}$$

Since the disturbance inputs by definition are assumed small, the cross-coupling terms involving the multiplication of two inputs are assumed to be negligible. Additionally small angle approximations are used for the disturbance pitch and bank angles($\Delta\theta$ and $\Delta\phi$) and the reference value of the pitch angle(θ_0) is the trimmed angle of attack of the aircraft(assuming no wind).

For the purposes of comparing the relative stability and controllability of the aircraft to other aircraft, as well as comparing results to vortex lattice code results, it is necessary to generalize these derivatives by nondimensionalizing them. The formulas used to nondimensionalize the derivatives are shown in Tables 3.3 and 3.4 [9, pp. 118,207] and are based on Buckingham's π theorem. The values

	C_x	C_z	C_m
u	$\frac{X_u}{\frac{1}{2}\rho u_0 S}$	$\frac{Z_u}{\frac{1}{2}\rho u_0 S}$	$\frac{M_u}{\frac{1}{2}\rho u_0 \bar{c} S}$
α	$\frac{X_w}{\frac{1}{2}\rho u_0 S}$	$\frac{Z_w}{\frac{1}{2}\rho u_0 S}$	$\frac{M_w}{\frac{1}{2}\rho u_0 \bar{c} S}$
Q	$\frac{X_q}{\frac{1}{4}\rho u_0 \bar{c} S}$	$\frac{Z_q}{\frac{1}{4}\rho u_0 \bar{c} S}$	$\frac{M_q}{\frac{1}{4}\rho u_0 \bar{c}^2 S}$
δ_e	$\frac{X_{\delta_e}}{\frac{1}{2}\rho u_0^2 S}$	$\frac{Z_{\delta_e}}{\frac{1}{2}\rho u_0^2 S}$	$\frac{M_{\delta_e}}{\frac{1}{2}\rho u_0^2 S \bar{c}}$

Table 3.3: Longitudinal Dimensionless Derivatives

	C_y	C_l	C_n
β	$\frac{Y_v}{\frac{1}{2}\rho u_0 S}$	$\frac{L_v}{\frac{1}{2}\rho u_0 b S}$	$\frac{N_v}{\frac{1}{2}\rho u_0 b S}$
P	$\frac{Y_p}{\frac{1}{4}\rho u_0 b S}$	$\frac{L_p}{\frac{1}{4}\rho u_0 b^2 S}$	$\frac{N_p}{\frac{1}{4}\rho u_0 b^2 S}$
R	$\frac{Y_r}{\frac{1}{4}\rho u_0 b S}$	$\frac{L_r}{\frac{1}{4}\rho u_0 b^2 S}$	$\frac{N_r}{\frac{1}{4}\rho u_0 b^2 S}$
δ_a	$\frac{Y_{\delta_a}}{\frac{1}{2}\rho u_0^2 S}$	$\frac{L_{\delta_a}}{\frac{1}{2}\rho u_0^2 S b}$	$\frac{N_{\delta_a}}{\frac{1}{2}\rho u_0^2 S b}$
δ_r	$\frac{Y_{\delta_r}}{\frac{1}{2}\rho u_0^2 S}$	$\frac{L_{\delta_r}}{\frac{1}{2}\rho u_0^2 S b}$	$\frac{N_{\delta_r}}{\frac{1}{2}\rho u_0^2 S b}$

Table 3.4: Lateral Dimensionless Derivatives

used to nondimensionalize the derivatives are the aircraft's wing area (S), mean aerodynamic chord ($\bar{c}$), wing span (b), trimmed forward velocity (u_0), and air density (ρ).

These nondimensional stability and control derivatives show the aircraft's static stability, as well as allow for determination of relative stability margin and control surface effectiveness to other known aircraft. The static stability of the aircraft is determined based on the sign of certain stability derivatives. For example C_{m_α}, describes the change in the aircraft's pitching moment for a given disturbance in α, this is commonly referred to as 'pitch stiffness'. An increase in α represents an increase in the aircraft's pitch angle, as such C_{m_α} must be negative to ensure that an increased pitch angle causes a negative pitching moment to counteract it. C_{n_β}, describes the change in the aircraft's yawing moment for a given disturbance in β. However, since a positive sideslip angle is conventionally defined as a negative rotation about the aircraft's z-axis a positive yawing moment is needed to correct it. As a result C_{n_β}, also known as 'weathercock stability', must be positive to be statically stable. The relative stability margin and control effectiveness of an

aircraft can be inferred by comparing its nondimensional derivative values to those of an aircraft with known stability and control effectiveness.

The key stability derivatives that will be used to model the angular rate dynamics of the aircraft are, C_{l_p}, $C_{l_{\delta_a}}$, C_{m_q}, $C_{m_{\delta_e}}$, C_{n_r}, and $C_{n_{\delta_r}}$. C_{l_p} and $C_{l_{\delta_a}}$ describe the effect a disturbance in roll rate and aileron deflection has on the rolling moment. C_{m_q} and $C_{m_{\delta_e}}$ describe the effect a disturbance in pitch rate and elevator deflection has on the pitching moment. C_{n_r} and $C_{n_{\delta_r}}$ describe the effect a disturbance in yaw rate and rudder deflection has on the yawing moment.

Chapter 4

Control Law Derivation

The stability and control derivatives calculated in Chapter 3 can now be used to calculate controller gains to be used with an attitude controller on board the aircraft. This chapter begins with a brief discussion of the control architecture used in this thesis. The control architecture used as a model for the calculations of the controller gains and the subsequent simulation of the aircraft's dynamics, is the fixed wing attitude controller included in the PX4 open-source autopilot stack, briefly discussed in Section 1.3. The goal is to input a desired damping ratio and natural frequency for the roll, pitch, and yaw rate inner control loops and output the controller gains required to fly the aircraft autonomously, without the need to further tune the gains. This is critical for modular aircraft since taking the time to re-tune the controller gains every time the aircraft's configuration is changed may not be feasible.

4.1 Controller Description

The fixed wing attitude controller included in the PX4 autopilot consists of PI controller loops around the roll, pitch, and yaw rates, as well as a proportional gain between the angle error and rate command for roll and pitch. This proportional gain is the inverse of a time-constant defined in the PX4 autopilot parameters, its purpose is to impose a latency between the commanded input and achieved set-point in order to protect control surface actuators from wearing out. For the purpose of these simulations the time-constant for both pitch and roll was set to

the PX4 autopilot default value of 0.5 seconds. There is also a direct feed-forward gain between the rate command and control surface deflection for all three rates, however this term is set to zero since the trimmed angular rates equal zero due to the steady, level flight trim condition. A block diagram representation of the controller is shown in Figure 4.1. This depiction is of generic form and applies to the roll and pitch dynamics. The yaw controller is of the same design except it does not include the angle controller, instead starting from a commanded rate set-point. The angle and rate feed-forward controllers are just proportional gains while the rate contoller is a PI controller of the form $K_{PI}(s) = K_P + \frac{K_I}{s}$. K_P and K_I are the rate proportional and integral gains respectively, they will be different for each controller and are calculated using the stability and control derivatives as well as desired controller performance criteria.

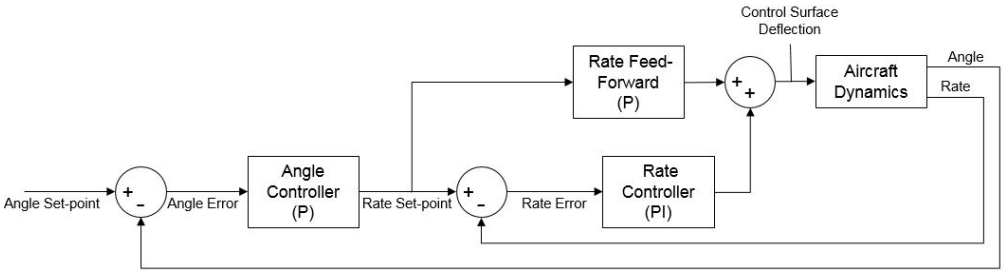

Figure 4.1: Controller Block Diagram

4.2 Controller Gain Calculation

Calculating the proportional and integral gains for the three rate PI controllers begins with the linearized moment equations for the aircraft. Since the inner-loop controller focuses on the angular rate dynamics, the terms relating to the angles (α and β) are dropped. Any errors caused by this omission can be corrected through the outer-loop proportional gain on the flight angles. In addition, the steady state terms live within the trim setting and any errors in calculating the trim setting will be handled by the integral term in the controller. Lastly, the coupling between roll and yaw dynamics (induced by the off-diagonal terms in the moment of inertia matrix) is ignored. The three simplified linear moment equations are

$$L = I_x \dot{P} = \frac{1}{2}\rho V_\infty^2 S\, b(C_{l_p} P + C_{l_{\delta_a}} \delta_a) \tag{4.1}$$

$$M = I_y \dot{Q} = \frac{1}{2}\rho V_\infty^2 S\, c(C_{m_q} Q + C_{m_{\delta_e}} \delta_e) \tag{4.2}$$

$$N = I_z \dot{R} = \frac{1}{2}\rho V_\infty^2 S\, b(C_{n_r} R + C_{n_{\delta_r}} \delta_r) \tag{4.3}$$

These equations are then transformed into transfer functions of the form $G(s) = \frac{Rate(s)}{Control(s)}$ by taking the Laplace transform of the equations and then separating terms. The resulting open loop transfer functions are

$$G_{roll}(s) = \frac{P(s)}{\delta_a(s)} = \frac{a_x C_{l_{\delta_a}}}{s - a_x C_{l_p}} \tag{4.4}$$

$$G_{pitch}(s) = \frac{Q(s)}{\delta_e(s)} = \frac{a_y C_{m_{\delta_e}}}{s - a_y C_{m_q}} \tag{4.5}$$

$$G_{yaw}(s) = \frac{R(s)}{\delta_r(s)} = \frac{a_z C_{n_{\delta_r}}}{s - a_z C_{n_r}} \tag{4.6}$$

where, $a_x = \frac{\frac{1}{2}\rho V_\infty^2 S\, b}{I_x}$, $a_y = \frac{\frac{1}{2}\rho V_\infty^2 S\, c}{I_y}$, and $a_z = \frac{\frac{1}{2}\rho V_\infty^2 S\, b}{I_z}$. Since a_x, a_y, and a_z are positive definite, a stable aircraft requires that C_{l_p}, C_{m_q}, and C_{n_r} are negative.

The expression for the closed loop transfer function of a system with feedback control, as shown in Figure 1.3, is given by

$$G_{CL}(s) = \frac{K(s)G_{OL}(s)}{1 + K(s)G_{OL}(s)} \tag{4.7}$$

where, $G_{OL}(s)$ is the open loop transfer function and $K(s)$ is the controller transfer function. For a PI controller the controller transfer function is given by $K_{PI}(s) = K_P + \frac{K_I}{s}$, where K_P is the proportional gain and K_I is the integral gain. The denominator of the closed loop transfer function is the characteristic equation of the system. Since the roots of the characteristic equation determine the behavior of the system the numerator can be ignored for the purpose of calculating the gains necessary to achieve the desired performance. The characteristic equations of the closed loop transfer functions for roll, pitch, and yaw are

$$1 + K_{PI_p} G_{roll} = s^2 + (K_{P_p} a_x C_{l_{\delta_a}} - a_x C_{l_p})s + K_{I_p} a_x C_{l_{\delta_a}} \tag{4.8}$$

$$1 + K_{PI_q} G_{pitch} = s^2 + (K_{P_q} a_y C_{m_{\delta_e}} - a_y C_{m_q})s + K_{I_q} a_y C_{m_{\delta_e}} \tag{4.9}$$

$$1 + K_{PI_r} G_{yaw} = s^2 + (K_{P_r} a_x C_{n_{\delta_r}} - a_z C_{n_r})s + K_{I_r} a_z C_{n_{\delta_r}} \tag{4.10}$$

In order to get a stable second-order system with damping ratio ξ and natural frequency ω_n the characteristic equation should take the form of $s^2 + 2\xi\omega_n s + \omega_n^2$. Since Equations 4.8 - 4.10 are already in this form, matching coefficients and solving for K_P and K_I yields the required controller gains to achieve a given damping ratio and natural frequency. The resulting equations for the controller gains in terms of stability and control derivatives are

$$K_{P_p} = \frac{2\xi\omega_n + a_x C_{l_p}}{a_x C_{l_{\delta_a}}} \tag{4.11}$$

$$K_{I_p} = \frac{\omega_n^2}{a_x C_{l_{\delta_a}}} \tag{4.12}$$

$$K_{P_q} = \frac{2\xi\omega_n + a_y C_{m_q}}{a_y C_{m_{\delta_e}}} \tag{4.13}$$

$$K_{I_q} = \frac{\omega_n^2}{a_y C_{m_{\delta_e}}} \tag{4.14}$$

$$K_{P_r} = \frac{2\xi\omega_n + a_z C_{n_r}}{a_z C_{n_{\delta_r}}} \tag{4.15}$$

$$K_{I_r} = \frac{\omega_n^2}{a_z C_{n_{\delta_r}}} \tag{4.16}$$

The design parameters of ω_n and ξ are chosen to achieve maximum performance while maintaining a realistically controllable system. For the purposes of this thesis a critically damped system with a damping ratio of 1 was assumed to ensure no oscillation. The natural frequency chosen is slightly more arbitrary, as a higher natural frequency will improve the response time of the system at the expense of increased control surface deflection. Too high of a control surface deflection will either stall the control surface or reach the physical limit of rotation. Figure 4.2

shows a simulation of the elevator response for a range of natural frequencies. The responses are to a commanded pitch angle of 10°. From the simulated results a natural frequency of 4 Hz was chosen as a good design point as there are diminishing returns in the settling time of the system for higher frequencies coupled with an increase in maximum control surface deflection. This method can be used to obtain natural frequencies for all controllers such that they meet performance criteria within the control surface deflection limits. As can be seen in Figures 4.3 and 4.4, a similar relationship between control surface response and natural frequency exists for the aileron and rudder.

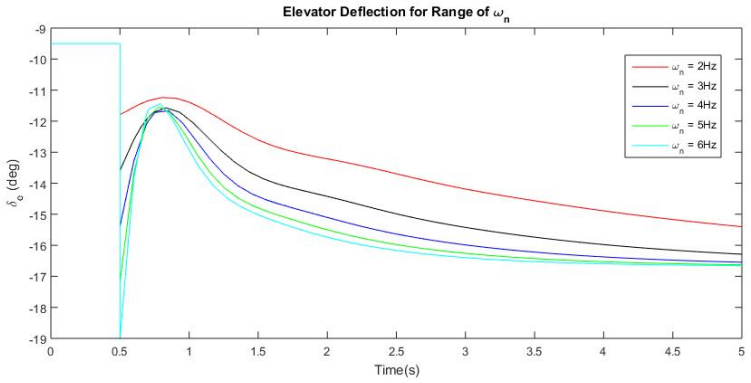

Figure 4.2: Elevator deflection for a range of ω_n

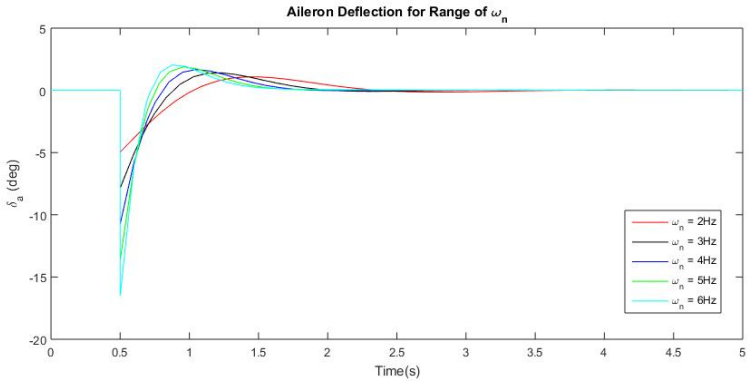

Figure 4.3: Aileron deflection for a range of ω_n

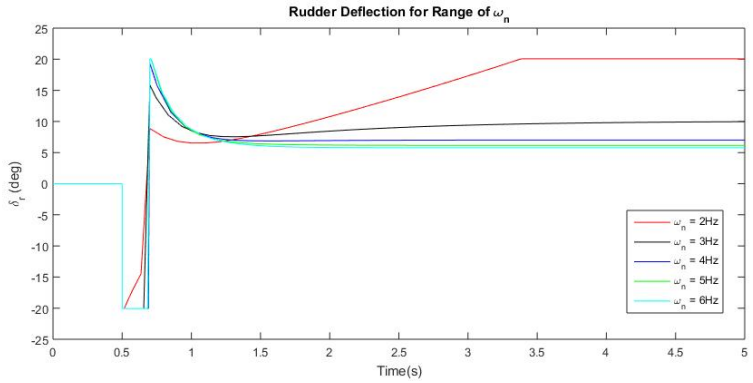

Figure 4.4: Rudder deflection for a range of ω_n

Chapter 5

Verification via Vortex Lattice Methods

The validity of the linearized aircraft model is checked by comparing the calculated stability and control derivatives to those calculated using a vortex lattice code for the same aircraft model. In this case the validation was done using Athena Vortex Lattice (AVL)[7].

5.1 AVL Aircraft Model Setup

In order to model the aircraft as similar as possible in AVL only lifting surfaces are included in the model. Therefore any fuselage, nacelle, or pods are ignored. While this may not model the aircraft as closely as it can, it can model the same surfaces as the strip model and therefore allow direct comparison of the methods. Non-lifting surfaces can be included in the strip model as long as force and moment data as functions of local velocity components are available. The airfoil section point files for each surface were included in the AVL model and the lift curve slopes were adjusted to match the values obtained from Xfoil. These inclusions were made in order to try and match the airfoil performance as best as possible between the models. All sections use cosine spacing both chordwise and spanwise, as this allows for more detail to be captured at the leading and trailing edges of the surfaces as well as at the tips of surfaces. This comes at the disadvantage of computational cost since there will be extra vortices placed at section tips even if they are connected

to another section and don't require extra fidelity at that location. The number of vortices used both spanwise and chordwise depends on the size of the section and may need to be adjusted to get the best combination of computation speed and model accuracy. Another note about the creation of the AVL model is that the coordinate system origin is centered at the leading edge of the main wing rather than the center of gravity (CG) of the aircraft. This enables the user to specify the location of the CG so that it can be easily moved to reflect aircraft design changes.

5.2 Model Validation Tests

The flight conditions used for both the AVL model and strip model were identical in order to minimize sources of error. The flight conditions used for the tests described in Sections 5.2.1 - 5.2.3 were an airspeed of 15 $\frac{m}{s}$ and air density of 1.225 $\frac{kg}{m^3}$. The CG location for each case was set to the same value of 0.070 m aft of the main wing leading edge. This is not necessarily representative of where the actual CG would be located on any of these aircraft, but was done for simplicity in creating the strip model. In addition, these tests are to compare the strip model to AVL and not to test the capabilities of a particular design. So as long as both methods are modeling the same aircraft geometry under the same flight conditions, the tests are valid. The AVL model was set up to run a longitudinally trimmed flight condition, this involved setting the angle of attack to achieve a desired aircraft C_L of 0.6 and commanding the elevator deflection angle to drive the pitching moment to zero. This results in a trimmed angle of attack and elevator deflection that are then used for the baseline flight condition of the strip model.

Since the strip model's primary function is calculating the PI controller gains for the inner, angular rate control loops, we need only focus on the derivatives that govern the linear moment dynamics as used in calculating the controller gains(See Section 4.2, Equations 4.1, 4.2, and 4.3). These key derivatives are C_{l_p}, $C_{l_{\delta_a}}$, C_{m_q}, $C_{m_{\delta_e}}$, C_{n_r}, and $C_{n_{\delta_r}}$. If the strip model is able to calculate these key derivatives to within an acceptable level of error compared to the AVL derivatives, then the model can be considered accurate for the purpose of calculating the inner-loop controller gains.

5.2.1 3 Wing Segments, 2 Tails

The first test case involves an aircraft with three 16" x 16" wing segments, two horizontal all-flying tails, and four vertical fins on either side of the horizontal tails. The vertical fins on the right side of each horizontal tail have conventional rudders with the hinge located at 70% of the chord. The geometry plot of the AVL model is shown in Figure 5.1. The model shows the geometric layout of the aircraft as well as the locations of vortex distributions. The trimmed α and δ_e for this test case are 7.29° and $-9.5°$, respectively.

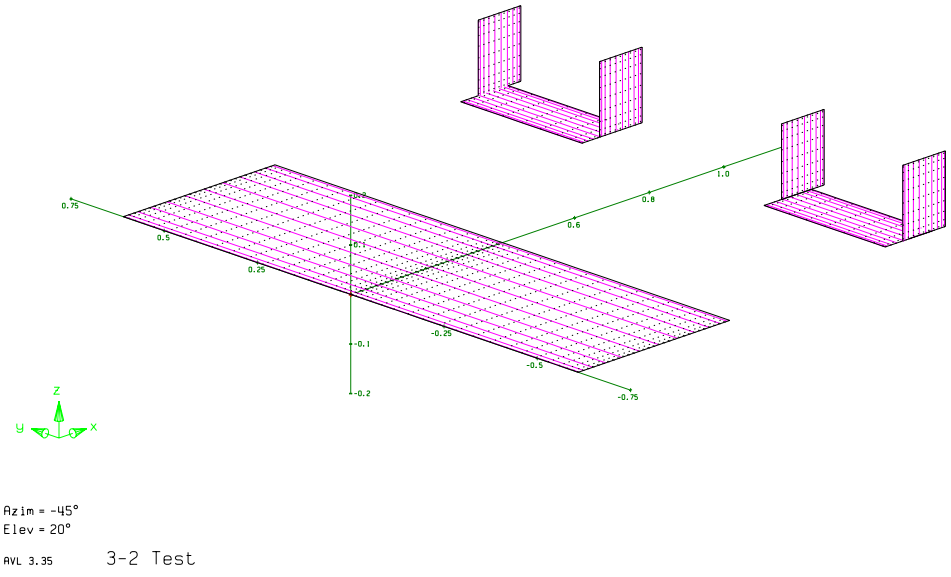

Figure 5.1: 3 Wing Segment, 2 Tail AVL Model

The comparison of the stability and control derivatives calculated by AVL and the strip model for this test case can be seen in Table 5.1. One of the main shortfalls of the strip method is its reliance on lifting-line theory, which is not valid for small aspect ratios (< 4). Since the vertical tails have a small aspect ratio (≈ 1) it can be inferred that the strip model will not accurately predict their behavior. In addition for this particular case, the trailing vortices of the wingtips will interact with the

outermost vertical tails. This effect is captured in the AVL model, but not in the strip model. This can be seen with the rudder control derivative, which differs by more than 100%. Since the key derivatives have small relative errors, the strip model can be considered valid for this configuration. The only concern is $C_{n_{\delta_r}}$ since it has a large error, however since the magnitude is small it is acceptable. It is important to note that the strip model predicts the rudder power to be approximately twice the value that AVL predicts. A possible cause to this is the difference in how AVL handles control surface deflections. The strip model uses viscous Xfoil data for various flap deflections to predict the changes in aerodynamic properties of a surface due to a control surface deflection. AVL documentation does not mention how control surfaces are handled, however given that AVL only uses the airfoil profile data to construct a camber line it is safe to assume that it modifies this camber line, using an user-defined flap hinge location, to simulate the effect of a control surface. This difference coupled with the inaccuracy of the strip model with low aspect ratio surfaces, as well as the absence of the trailing vortex effect, are likely the cause of the large error in the rudder control derivative.

Derivative	AVL	Strip Model	% Difference
C_{l_p}	-0.3319	-0.3805	14.7
$C_{l_{\delta_a}}$	-0.0029	-0.0030	3.7
C_{m_q}	-4.8200	-4.2151	12.6
$C_{m_{\delta_e}}$	-0.0175	-0.0181	3.2
C_{n_r}	-0.2780	-0.2990	7.6
$C_{n_{\delta_r}}$	-0.0012	-0.0025	104.8

Table 5.1: Key Stability and Control Derivative Comparison for 3 Segment, 2 Tail Configuration

5.2.2 5 Wing Segments, 2 Tails

The second test case is for the same configuration as the first, only with one more wing segment added on each side of the main wing. The geometry plot of the AVL model is shown in Figure 5.2. The trimmed α and δ_e for this test case are 5.0° and $-14.0°$ respectively.

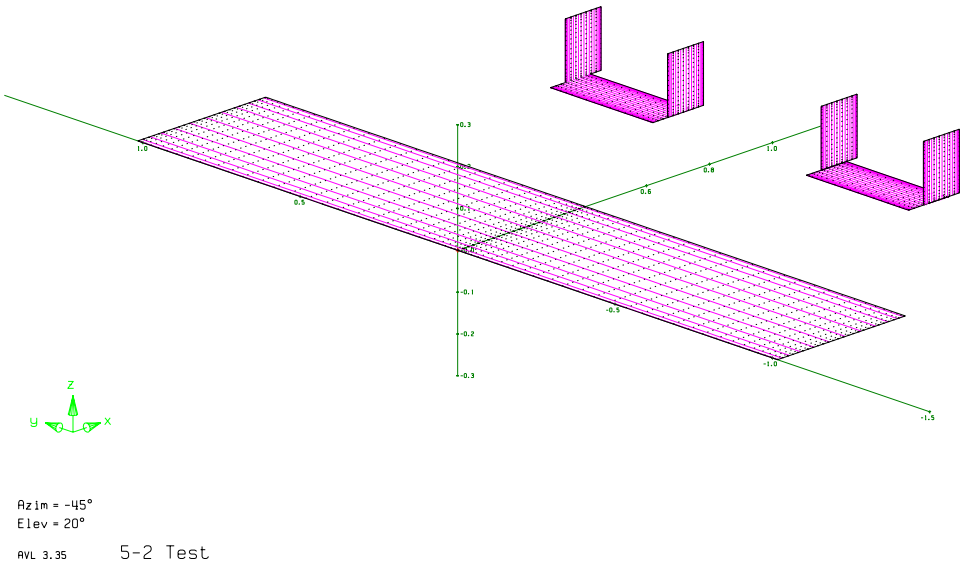

Figure 5.2: 5 Wing Segment, 2 Tail AVL Model

The results for this test case, shown in Table 5.2, are similar to the first case. The small aspect ratio of the vertical fins as well as the small rudder control surface area, leads to larger errors in the derivatives with contributions from these surfaces. Again for the purpose of calculating the controller gains these errors are within acceptable margins and as such the strip model is valid for this case. An interesting thing to note is that the error in C_{n_r} for this case dropped significantly as compared to the first case. This is likely due to the vertical tails no longer having the influence of the wingtip vortices due to the extended wing span.

Derivative	AVL	Strip Model	% Difference
C_{l_p}	-0.4040	-0.4345	7.5
$C_{l_{\delta_a}}$	-0.00107	-0.00106	0.8
C_{m_q}	-3.3621	-2.4861	26.1
$C_{m_{\delta_e}}$	-0.0106	-0.0107	0.8
C_{n_r}	-0.0609	-0.0615	1.0
$C_{n_{\delta_r}}$	-0.00043	-0.00088	102.0

Table 5.2: Key Stability and Control Derivative Comparison for 5 Segment, 2 Tail Configuration

5.2.3 5 Wing Segments, V-Tail

The third test case involves the same five segment wing as case two, however the two all-flying horizontal tails and four vertical fins have been replaced with a v-tail. The v-tail contains traditional control surfaces with hinges at 70% chord that act as ruddervators. Ailerons have been added to the two wing segments on either side of the center section with hinges also at 70% chord. The AVL geometry plot for this test case can be seen in Figure 5.3. The trimmed α and δ_e for this test case are $4.76°$ and $-9.41°$ respectively.

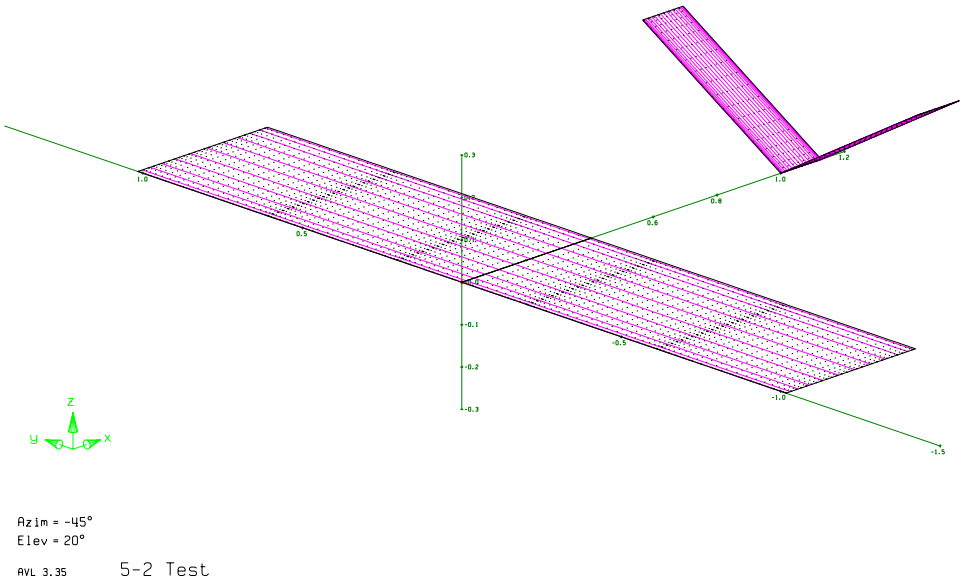

Figure 5.3: 5 Wing Segment, V Tail AVL Model

The comparative results for test case three can be found in Table 5.3. As can be seen from the results, since the amount of rudder area increased the rudder control derivative error decreased. Since there are no longer vertical tail surfaces, the stability derivatives dependent on them did not improve in accuracy. The necessary derivatives to simulate the rate dynamics are all within acceptable margins and therefore this test case shows the model to be valid for this purpose.

Derivative	AVL	Strip Model	% Difference
C_{l_p}	-0.4007	-0.4260	6.3
$C_{l_{\delta_a}}$	-0.0029	-0.0036	22.6
C_{m_q}	-6.9729	-5.6870	18.4
$C_{m_{\delta_e}}$	-0.0175	-0.0156	11.3
C_{n_r}	-0.0546	-0.0670	22.8
$C_{n_{\delta_r}}$	-0.0014	-0.0017	21.0

Table 5.3: Key Stability and Control Derivative Comparison for 5 Segment, V Tail Configuration

5.3 Comparative Simulation of Controller Response

In order to test the performance of the controller calculated by the strip model, it will be compared to the performance of a controller calculated using AVL's stability and control derivatives. This comparison is done for each of the three test cases described in Section 5.2. In order to compare just the controller performance the simulations will use the aircraft's dynamics models with AVL stability and control derivatives for both controllers. Since the vortex lattice method is a more accurate model of aircraft aerodynamic properties its results will be taken to be the model of how the actual aircraft will respond in flight. As for the simulation conditions, the baseline will be the longitudinal trim condition with V_∞ of 15 $\frac{m}{s}$ and ρ of 1.225 $\frac{kg}{m^3}$. The geometry parameters as well as the trim values for α and δ_e for each test case are shown in Table 5.4. In this case since the goal is just to validate against the AVL model and not necessarily predict real aircraft behavior, a rough approximation for the moments of inertia was used. In each case, each surface was modeled as a solid plastic airfoil, this creates an aircraft with much higher moments of inertia than are realistic. However since the same ones are used for both controllers it will not effect the result. This will affect the aircraft simulation model however, the closer the moments of inertia get to the actual value for an aircraft the more accurate that simulation becomes in predicting aircraft response.

A Simulink block diagram of each of the controllers as they are implemented in the autopilot are shown in Figures 5.4 - 5.6. Each of these models also includes a linear model of the aircraft's dynamics for the purpose of simulating aircraft response

to the control inputs and gain approximate knowledge of how the controller will perform in flight. Since the roll and pitch controllers have an outer loop controlling the attitude angles, the control inputs for them are a step input of 10° of commanded attitude angle change from the baseline trim condition. The yaw rate loop's control input is a commanded yaw rate pulse of 0.175 $\frac{rad}{s}$ with a pulse width of 0.2 seconds.

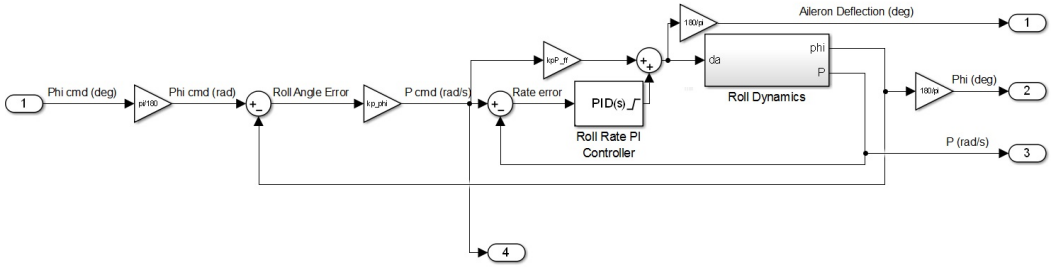

Figure 5.4: Simulink Model of the Roll Rate Controller

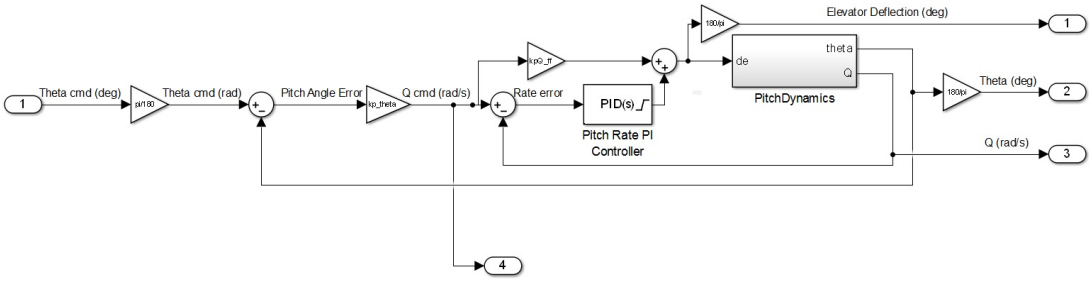

Figure 5.5: Simulink Model of the Pitch Rate Controller

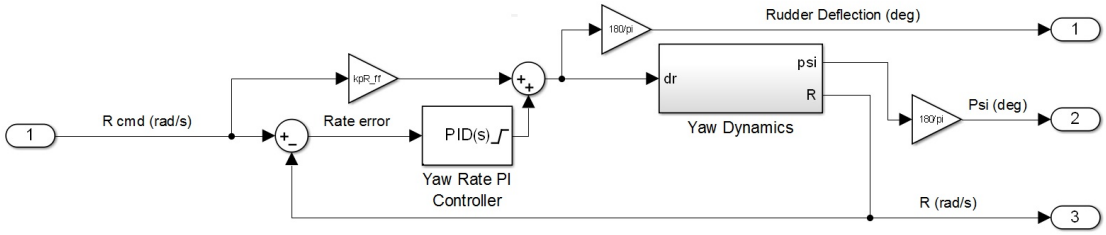

Figure 5.6: Simulink Model of the Yaw Rate Controller

The Simulink block diagrams of each linear aircraft dynamics model are shown in Figures 5.7 - 5.9. The linear aircraft dynamics are based on Equations 4.1, 4.2, and 4.3. Since these simulations are done with respect to a single axis of motion at a time, it can be assumed that the components with respect to other axes are negligible.

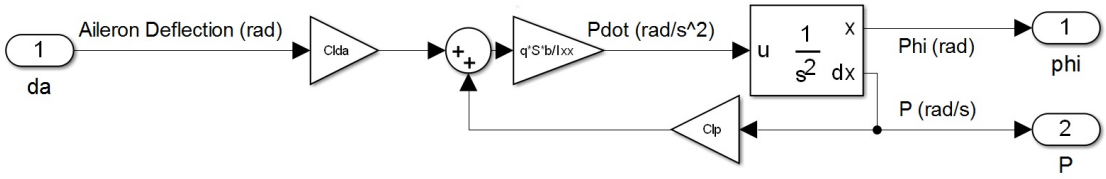

Figure 5.7: Simulink Model of the Linear Aircraft Roll Dynamics

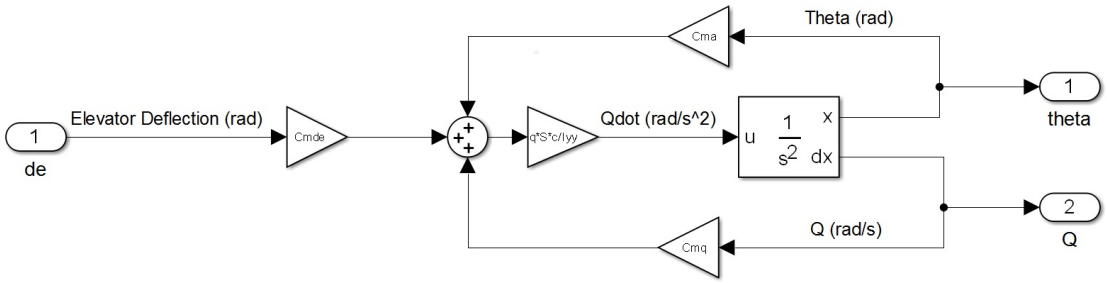

Figure 5.8: Simulink Model of the Linear Aircraft Pitch Dynamics

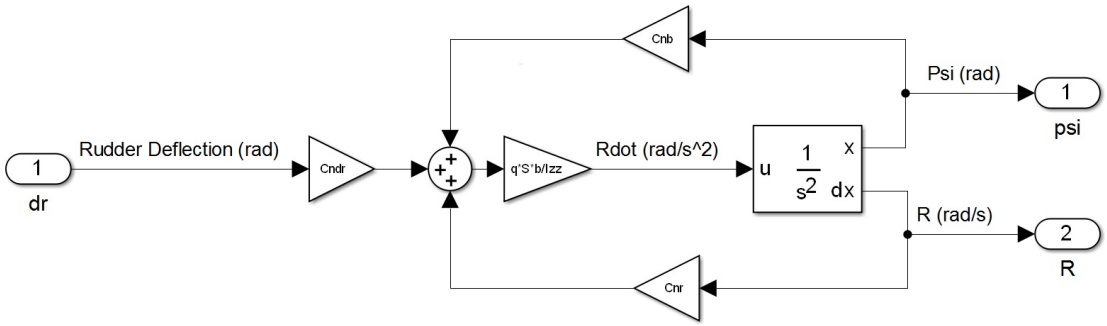

Figure 5.9: Simulink Model of the Linear Aircraft Yaw Dynamics

The geometric parameters as well as the α and δ_e values required to trim the aircraft for the three test cases are shown in Table 5.4. The trim values are obtained from AVL using the method described in Section 5.2.

Test Case	3 Wing Seg, 2 Tails	5 Wing Seg, 2 Tails	5 Wing Seg, V-Tail
$S\ (m^2)$	0.4956	0.8258	0.8258
$c\ (m)$	0.4064	0.4064	0.4064
$b\ (m)$	1.2192	2.0320	2.0320
$I_x\ (kg \cdot m^2)$	1.97	8.24	8.09
$I_y\ (kg \cdot m^2)$	1.25	1.42	1.72
$I_z\ (kg \cdot m^2)$	3.21	9.64	9.75
$\alpha_{trim}\ (^\circ)$	7.29	5.00	4.76
$\delta_{e,trim}\ (^\circ)$	-9.55	-14.01	-9.41

Table 5.4: Test Case Geometry and Trim Conditions

The design parameters used to calculate the controller gains for all cases were $\omega_n = 4\ Hz$ and $\xi = 1$. Making the system critically damped ($\xi = 1$) removes oscillations in the system response. The natural frequency of 4 Hz was more arbitrarily chosen as a value that yielded adequate performance in all cases, as previously discussed in Section 4.2. These simulations are only a comparison of the strip model controller's performance relative to the AVL baseline, and do not attempt to find an optimal controller.

Since the basis for both of these models is small disturbance theory with a baseline trimmed condition, it is important to note that all resulting values from the simulations are Δ's from that respective case's trimmed values.

5.3.1 Test Case 1

The first test case is the three wing segment, two all-flying tail configuration. The controller gains calculated for this test case for both the strip model controller and the AVL controller are shown in Table 5.5. The gains for both sets of controllers are very similar except for the yaw rate controllers which is due to the large relative error from the rudder control derivatives as described in Section 5.2.1.

	Strip Model Controller	AVL Controller
K_{P_p}	-1.022	-1.073
K_{I_p}	-2.226	-2.310
K_{P_q}	-0.293	-0.294
K_{I_q}	-0.697	-0.718
K_{P_r}	-2.112	-4.321
K_{I_r}	-4.396	-8.971

Table 5.5: Test Case 1 PI Controller Gains

The results from the simulations for Case 1 are shown in Figures 5.10 - 5.13. Each figure shows the response of its particular variable for systems with both the strip model controller and the AVL controller. As can be seen from the results the only responses that don't line up completely are the yaw rate response and the rudder deflection response as was expected. However the yaw rate response, which is the more important of the two since it is a directly controlled variable, only shows a slightly more lagged response. The behavior shown for the yaw rate is still stable and would not have a profound effect on overall aircraft performance.

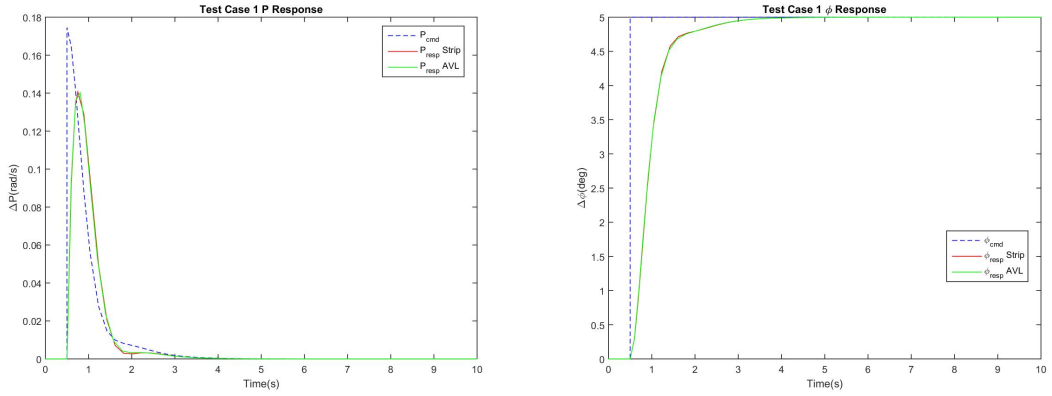

(a) Roll Rate Response (b) Roll Angle Response

Figure 5.10: Case 1 Roll Response

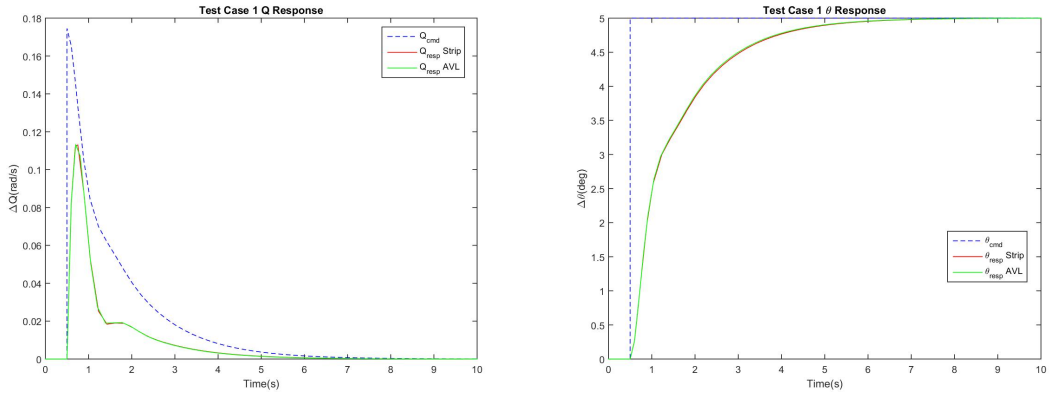

(a) Pitch Rate Response (b) Pitch Angle Response

Figure 5.11: Case 1 Pitch Response

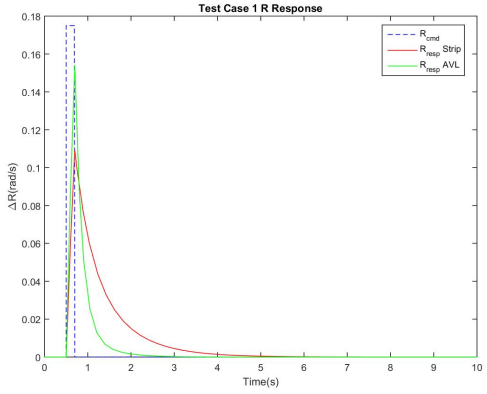

Figure 5.12: Yaw Rate Response

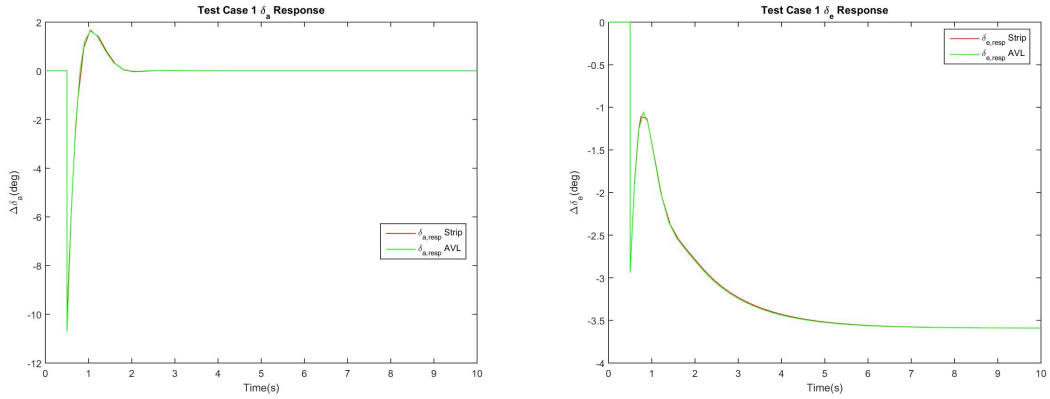

(a) Aileron Response

(b) Elevator Response

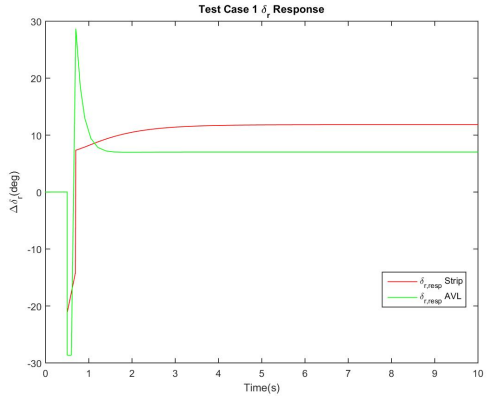

(c) Rudder Response

Figure 5.13: Case 1 Control Surface Response

5.3.2 Test Case 2

The second test case is the five wing segment, two all-flying tail configuration. The controller gains calculated for this test case for both the strip model controller and the AVL controller are shown in Table 5.6. Again the gains for roll and pitch are nearly identical and the gains for yaw differ similarly to Case 1. This again can be traced back to the rudder control derivative issue.

	Strip Model Controller	AVL Controller
K_{P_p}	-4.211	-4.202
K_{I_p}	-9.391	-9.297
K_{P_q}	-0.346	-0.330
K_{I_q}	-0.803	-0.809
K_{P_r}	-6.575	-13.37
K_{I_r}	-13.32	-27.07

Table 5.6: Test Case 2 PI Controller Gains

The results from the simulations for Case 2 are shown in Figures 5.14 - 5.17. Similar to the first case, there is very little error in the roll and pitch dynamics. There is still some error in the yaw dynamics, however not as much as the first case. This is most likely due to the increase in z-axis moment of inertia of this aircraft configuration while maintaining the same rudder surface area. Even though AVL predicts the rudders to be half as effective as the strip model does, for this configuration they are both so under-powered that the effect on the dynamics is negligible. This can be seen when comparing Figures 5.13c and 5.17c. In Figure 5.13c the response of the rudder for the AVL controller hits the lower saturation limit while the strip model controller response does not. In Figure 5.17c the responses of both controllers hit the saturation limit showing that there was not enough rudder control authority to get to the commanded yaw rate in either case.

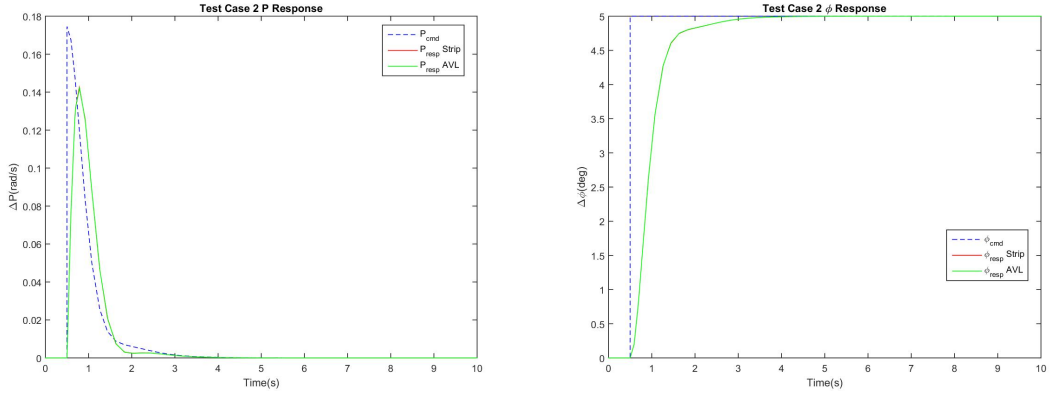

(a) Roll Rate Response (b) Roll Angle Response

Figure 5.14: Case 2 Roll Response

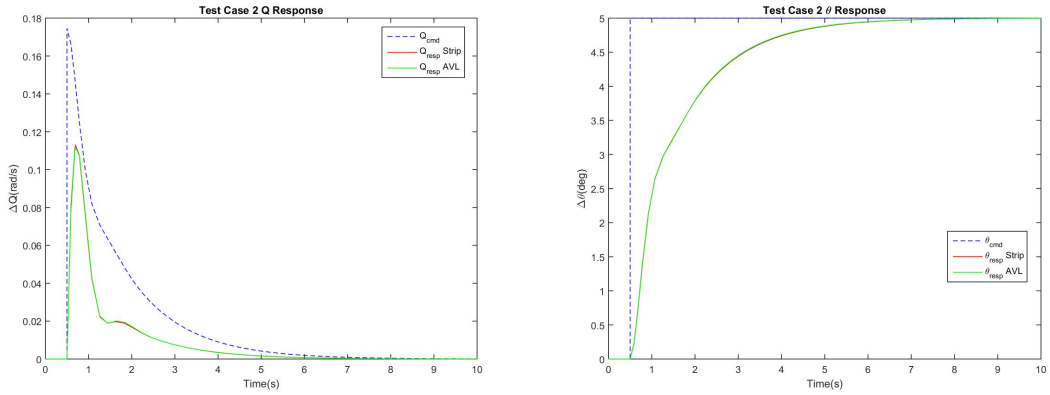

(a) Pitch Rate Response (b) Pitch Angle Response

Figure 5.15: Case 2 Pitch Response

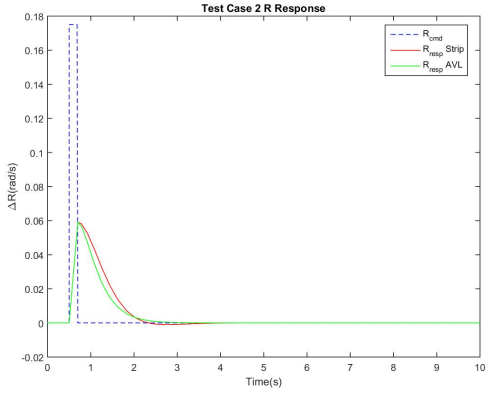

Figure 5.16: Case 2 Yaw Rate Response

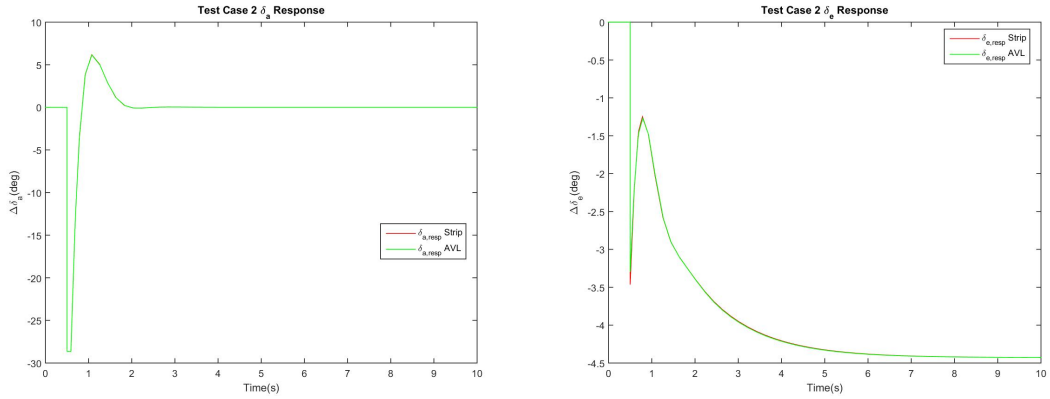

(a) Aileron Response

(b) Elevator Response

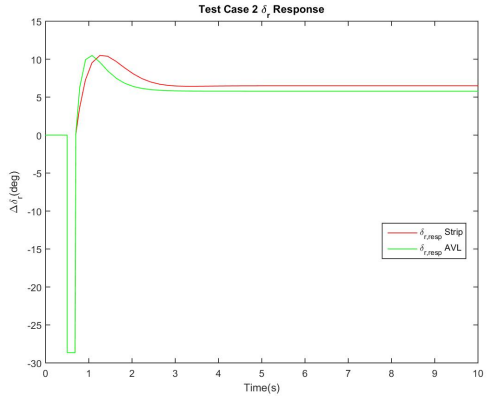

(c) Rudder Response

Figure 5.17: Case 2 Control Surface Response

5.3.3 Test Case 3

The third test case is the five wing segment, v-tail configuration. The controller gains calculated for this test case for both the strip model controller and the AVL controller are shown in Table 5.7. In this case the relative error for the yaw controller gains is much smaller than in the previous two cases. This is primarily due to the reduction in the rudder control derivative error discussed in Section 5.2.3.

	Strip Model Controller	AVL Controller
K_{P_p}	-1.250	-1.541
K_{I_p}	-2.781	-3.407
K_{P_q}	-0.189	-0.150
K_{I_q}	-0.551	-0.489
K_{P_r}	-3.326	-4.024
K_{I_r}	-6.744	-8.139

Table 5.7: Test Case 3 PI Controller Gains

The results from the simulations for Case 3 are shown in Figures 5.18 - 5.21. Since the stability and control derivatives and subsequently the controller gains with respect to yaw contain much less error in this case than the two previous cases the yaw responses of both controllers should in turn be much more closely aligned. As can be seen in Figures 5.20 and 5.21c the responses are much more similar and have about the same amount of error as the roll and pitch responses. It should be noted that in 5.21c both responses again hit the saturation limit, suggesting not enough rudder authority to meet the rate set point. Again since this is primarily a comparative test to compare the strip model to AVL this is not a concern.

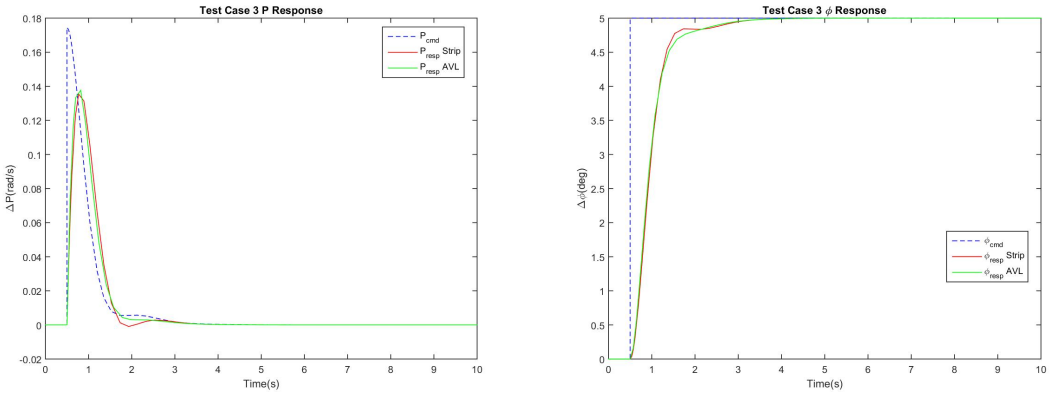

(a) Roll Rate Response

(b) Roll Angle Response

Figure 5.18: Case 3 Roll Response

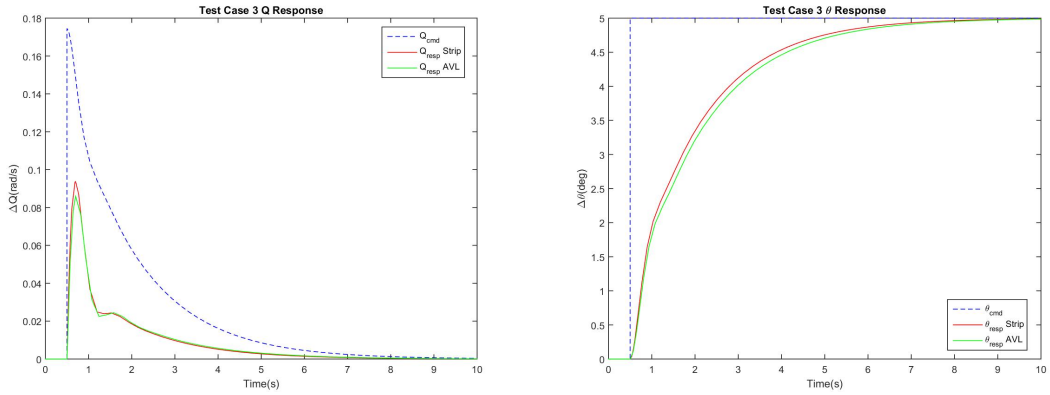

(a) Pitch Rate Response (b) Pitch Angle Response

Figure 5.19: Case 3 Pitch Response

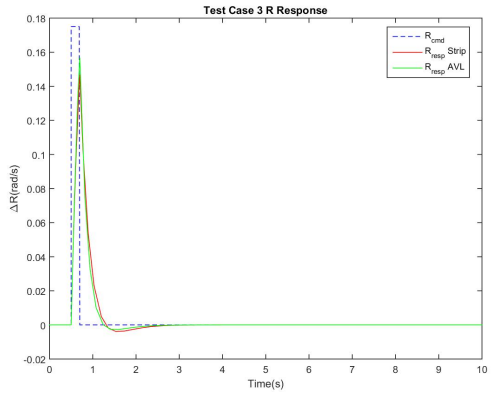

Figure 5.20: Case 3 Yaw Rate Response

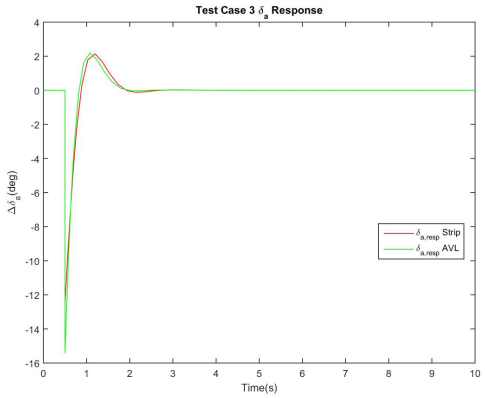

(a) Aileron Response

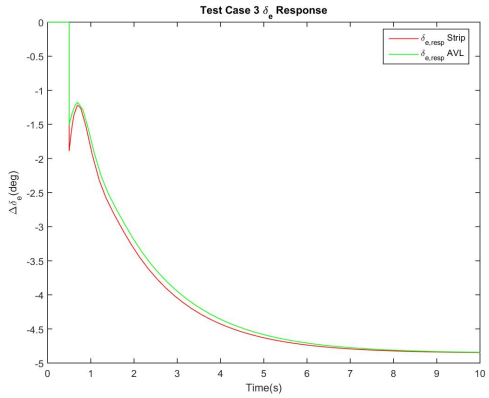

(b) Elevator Response

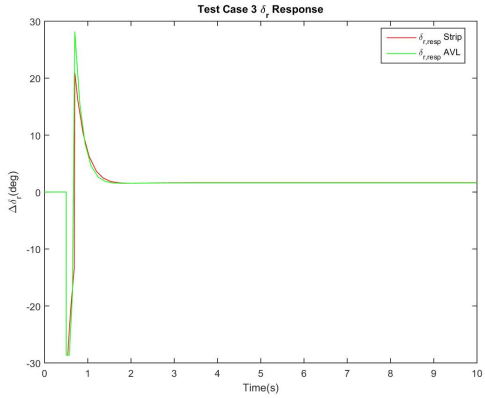

(c) Rudder Response

Figure 5.21: Case 3 Control Surface Response

Chapter 6

Conclusions

The main purpose of this thesis was to develop a method in which controller gains compatible with the PX4 autopilot software could be quickly determined with minimal computational expense for a modular uninhabited air vehicle. Being able to quickly and easily calculate the necessary gains needed to autonomously fly any given configuration of a modular vehicle is essential in maintaining flexibility and responsiveness in the field.

The controller gains were calculated assuming a PI controller and a linear plant model for the roll, pitch, and yaw angular rates. The linear plant models used the applicable stability and control derivatives for the roll, pitch, and yaw moment dynamics. These stability and control derivatives were derived from linearizing the equations of motion of the aircraft about a steady, longitudinally trimmed flight condition. The most common way of determining the stability and control derivatives for a given aircraft accurately is to use the numerical vortex lattice method to simulate the aircraft's aerodynamic properties. The vortex lattice method is computationally expensive and requires creating a new model for each aircraft configuration. The method used to simplify the calculations of the stability and control derivatives was to break the aircraft's aerodynamic surfaces up into discrete section. The forces and moments acting on each individual section are calculated using a 2D approximation which is then modified using lifting-line theory to account for 3D effects. These section equations of motion are then linearized with respect to the desired trim condition and then summed about the aircraft's center of gravity. This results in the dimensional stability and control derivatives

for the aircraft, which are then non-dimensionalized to be used in the calculation of the controller gains or to model the aircraft for simulation.

6.1 Results

The goal for testing of the strip model was to show that it can quickly and accurately produce similar results to vortex lattice code for the purpose of calculating controller gains for autonomous flight. The specific vortex lattice code used for the comparison was AVL[7]. The time to run an AVL case for a single configuration is on the order of a minute, which does not include the time needed to generate the model. The strip model, on the other hand, calculates the stability and control derivatives and the required inner-loop controller gains nearly instantaneously. When posed with the possibility of hundred's of individual configurations, the strip model is the preferred method.

Three test cases were used to test the fidelity of the strip model against AVL. The first, incorporated three wing sections, two all-flying horizontal tails, and four vertical tails. The second, had five wing sections and the same tail setup as the first case. The last test case had five wing sections and a v-tail.

Two comparisons were made between the strip model and the AVL model. The first was a comparison of the stability and control derivatives calculated using the two models. The second was a comparison of the simulated response of the aircraft to a disturbance with each respective controller implemented. The simulation results are the more important of the two, as they directly compare the actual response of controllers designed using each model. It is still important to look at the error in the derivatives themselves in the context of explaining the discrepancies in the simulation results. However, the ultimate goal was to show that a controller designed with the strip model behaves the same as one designed using AVL. This allows for the use of the strip model in calculating autopilot controller gains quickly as aircraft configurations are changed in the field, or when determining viability of a large set of configurations.

The results of the simulations, which can be seen in Chapter 5, show that for all three cases the roll and pitch response show little to no relative error between the strip model controller and the AVL controller. The yaw rate response shows more relative error, particularly with the first case. However, since the rudders

are undersized for this case and yaw control is secondary to roll and pitch in autonomous flight, the controller designed with the strip model can be seen as a suitable controller to use for these configurations. In addition, since the three test cases contained a variety of different surface types and control configurations, this model should be accurate for most 'typical' aircraft configurations. Exceptions to this are discussed in Section 6.2.

6.2 Sources of Error

The discrepancy in the yaw performance as discussed earlier is caused by the strip model calculating the rudder control derivatives to be approximately two times the value of the derivatives calculated by AVL. The reason for this discrepancy is unknown. One likely cause is the low aspect ratio of the vertical tails, which pushes the limits of the lifting-line theory approximations used in calculating the forces and moments of the surfaces. Another possible cause is the difference in how the effect of a control surface is handled in the strip model vs AVL. The strip model uses a viscous panel method simulation at the operating Reynolds number for various control surface deflection angles. This creates a model of the effect of control surface deflection on the lift and moment coefficients of the airfoil. It is unknown how AVL calculates control surface effects but it likely has to do with a modification of the camber line, or perhaps a generic modification to the airfoil properties that is used on all control surfaces. For normally sized control surfaces in normal application this difference is negligible, as can be seen with case 3 where the ailerons and ruddervators have similar control derivative predictions across both models. However with the combination of low surface aspect ratio and small control surface size these errors cascade to create the large difference seen.

In addition to errors noted in the simulated cases, this model will most likely lose accuracy with certain aircraft configurations. For instance the strip model only looks at lifting surfaces, so any fuselage, nacelle, or pod is not modeled aerodynamically. For most cases these terms would be negligible, however for a large circular fuselage the drag due to side-slip would have a significant influence on the C_{y_β} and C_{n_β} derivatives. It is possible to include the effects of non-lifting surfaces if equations for the aerodynamic forces and moments in terms of local velocities can be determined. Another effect that is not modeled is any one surface's

effect on any surfaces downstream. For configurations where surfaces are far apart or elevated above upstream surfaces this effect will be negligible. If surfaces are tightly grouped together the model will most likely lose accuracy. While dihedral and twist can be modeled in the strip model, sweep can not. So this model can only be used for straight-winged aircraft. It would be possible to include z-axis rotation of strips in the model, however further testing would be required to determine if that alone can accurately model the effects of sweep.

Neither AVL nor the strip model are accurate when it comes to the drag calculations. To simplify the model, and knowing the drag would be inaccurate regardless, induced drag is not included in the strip model. The only drag effect in the strip model is the viscous profile drag calculated by Xfoil. AVL calculates the induced drag, but has no method for determining profile drag. For the calculation of the controller gains the contributions from the drag are negligible compared to those of the lift and moment. If an accurate aerodynamic model is desired for use in a flight simulator another method should be used to approximate the drag.

6.3 Future Work

Areas for future improvements to this model include, using a more comprehensive aerodynamic model in simulation, validating results with flight tests. The model can also be embedded into optimization software that can determine optimal aircraft configurations for a given mission profile. The stability and control derivatives calculated by the strip model can be used to model the aircraft in a commercial flight simulator such as X-Plane or Flight Gear. This will allow hardware-in-the-loop simulations to get a better understanding of controller performance before flight tests. However, as mentioned previously the drag calculations in the strip model are inaccurate. Thus, a more accurate drag model will need to be used in order to more effectively model the aircraft in a flight simulator. The ultimate goal is inclusion of the strip model in a 'self-identifying' modular UAV. This aircraft could potentially use section microprocessors, as well as an on-board central flight computer, to determine its own configuration. With knowledge of the configuration the flight computer can run the strip model to determine its required controller gains. Once these gains are determined, they can be uploaded to the autopilot software enabling autonomous flight with minimal user input.

Appendix A

B and D Matrix Components

This Appendix contains all of the equations for the individual elements of the D and U matrices for both a traditional surface as well as an "All-Flying" surface. The elements described below belong to the equation:

$$\begin{bmatrix} \Delta F_x^i \\ \Delta F_y^i \\ \Delta F_z^i \\ \Delta M_x^i \\ \Delta M_y^i \\ \Delta M_z^i \end{bmatrix} = \frac{1}{2}\rho S_i \left(\begin{bmatrix} D_{11}^i & D_{12}^i & D_{13}^i & D_{14}^i & D_{15}^i & D_{16}^i \\ D_{21}^i & D_{22}^i & D_{23}^i & D_{24}^i & D_{25}^i & D_{26}^i \\ D_{31}^i & D_{32}^i & D_{33}^i & D_{34}^i & D_{35}^i & D_{36}^i \\ D_{41}^i & D_{42}^i & D_{43}^i & D_{44}^i & D_{45}^i & D_{46}^i \\ D_{51}^i & D_{52}^i & D_{53}^i & D_{54}^i & D_{55}^i & D_{56}^i \\ D_{61}^i & D_{62}^i & D_{63}^i & D_{64}^i & D_{65}^i & D_{66}^i \end{bmatrix} \begin{bmatrix} \delta u_i \\ \delta v_i \\ \delta w_i \\ \delta P_i \\ \delta Q_i \\ \delta R_i \end{bmatrix} + \begin{bmatrix} U_1^i \\ U_2^i \\ U_3^i \\ U_4^i \\ U_5^i \\ U_6^i \end{bmatrix} \delta_i \right)$$

A.1 Section with "All-Flying" Control Surface

$$w_i = u_0 \sin\theta_i + w_0 \cos\phi_i \cos\theta_i \tag{A.1}$$

$$u_i = u_0 \cos\theta_i - w_0 \cos\phi_i \sin\theta_i \tag{A.2}$$

$$V_0^2 = u_0^2 + w_0^2 \tag{A.3}$$

$$\alpha_i = \delta_0 + \frac{w_i}{u_i} \tag{A.4}$$

$$A = C_{L0,i} + \alpha_i \left(C_{D0,i} + C_{L\alpha,i}\right) \tag{A.5}$$

$$B = C_{D0,i} - \alpha_i \left(C_{L0,i} + C_{L\alpha,i}\,\alpha_i\right) \tag{A.6}$$

$$C = 2\,C_{L\alpha,i}\,w_i \;+\; (C_{L0,i} \;+\; 2\,C_{L\alpha,i}\,\delta_0)\,u_i \tag{A.7}$$

$$E = B\,\cos\theta_i \;+\; A\,\sin\theta_i \tag{A.8}$$

$$F = A\,\cos\theta_i \;-\; B\,\sin\theta_i \tag{A.9}$$

$$G = r_{y,i}\cos\phi_i \;+\; r_{z,i}\sin\phi_i \tag{A.10}$$

$$H = r_{y,i}\,w_0\cos\phi_i \;-\; r_{x,i}\,u_0\sin\phi_i \tag{A.11}$$

$$I \;= r_{z,i}\,u_0 \;-\; r_{x,i}\,w_0 \tag{A.12}$$

$$J \;= r_{x,i}\,u_0 \;+\; r_{z,i}\,w_0 \tag{A.13}$$

$$K = \frac{C\sin\theta_i}{u_i^3} \;+\; (C_{D0,i} \;+\; C_{L\alpha,i})\frac{\cos\theta_i}{u_i^2} \tag{A.14}$$

$$L = \frac{C\cos\theta_i}{u_i^3} \;-\; (C_{D0,i} \;+\; C_{L\alpha,i})\frac{\sin\theta_i}{u_i^2} \tag{A.15}$$

A.1.1 D Matrix Components

$$D_{11} = \;-\,(2\,u_0\,E \;+\; w_0\,\cos\phi_i\,V_0^2\,L) \tag{A.16}$$

$$D_{12} = \;-\,u_0\,\sin\phi_i\,V_0^2\,L \tag{A.17}$$

$$D_{13} = \;-\,(2\,w_0\,E \;-\; u_0\,\cos\phi_i\,V_0^2\,L) \tag{A.18}$$

$$D_{14} = \;-\,(2\,r_{y,i}\,w_0\,E \;-\; u_0\,G\,V_0^2\,L) \tag{A.19}$$

$$D_{15} = \;-\,(2\,I\,E \;+\; J\,\cos\phi_i\,V_0^2\,L) \tag{A.20}$$

$$D_{16} = 2\,r_{y,i}\,u_0\,E \;+\; H\,V_0^2\,L \tag{A.21}$$

$$D_{21} = \sin\phi_i\,(2\,u_0\,F \;-\; w_0\,\cos\phi_i\,V_0^2\,K) \tag{A.22}$$

$$D_{22} = \;-\,u_0\,\sin\phi_i^2\,V_0^2\,K \tag{A.23}$$

$$D_{23} = \sin\phi_i\,(2\,w_0\,F \;+\; u_0\,\cos\phi_i\,V_0^2\,K) \tag{A.24}$$

$$D_{24} = \sin\phi_i\,(2\,r_{y,i}\,w_0\,F \;+\; u_0\,G\,V_0^2\,K) \tag{A.25}$$

$$D_{25} = \sin\phi_i\,(2\,I\,F \;-\; J\,\cos\phi_i\,V_0^2\,K) \tag{A.26}$$

$$D_{26} = \;-\,\sin\phi_i\,(2\,r_{y,i}\,u_0\,F \;-\; H\,V_0^2\,K) \tag{A.27}$$

$$D_{31} = \;-\,\cos\phi_i\,(2\,u_0\,F \;-\; w_0\,\cos\phi_i\,V_0^2\,K) \tag{A.28}$$

$$D_{32} = u_0\,\cos\phi_i\,\sin\phi_i\,V_0^2\,K \tag{A.29}$$

$$D_{33} = \;-\,\cos\phi_i\,(2\,w_0\,F \;+\; u_0\,\cos\phi_i\,V_0^2\,K) \tag{A.30}$$

$$D_{34} = \;-\,\cos\phi_i\,(2\,r_{y,i}\,w_0\,F \;+\; u_0\,G\,V_0^2\,K) \tag{A.31}$$

$$D_{35} = -\cos\phi_i\,(2\,I\,F\;-\;J\,\cos\phi_i\,V_0^2\,K) \tag{A.32}$$

$$D_{36} = \cos\phi_i\,(2\,r_{y,i}\,u_0\,F\;-\;H\,V_0^2\,K) \tag{A.33}$$

$$D_{41} = -G\,(2\,u_0\,F\;-\;w_0\,\cos\phi_i\,V_0^2\,K) \tag{A.34}$$

$$D_{42} = V_0^2\,u_0\,\sin\phi_i\,G\,K \tag{A.35}$$

$$D_{43} = -G\,(2\,w_0\,F\;+\;u_0\,\cos\phi_i\,V_0^2\,K) \tag{A.36}$$

$$D_{44} = -G\,(2\,w_0\,r_{y,i}\,F\;+\;u_0\,G\,V_0^2\,K) \tag{A.37}$$

$$D_{45} = -G\,(2\,I\,F\;-\;\cos\phi_i\,V_0^2\,J\,K) \tag{A.38}$$

$$D_{46} = G\,(2\,u_0\,r_{y,i}\,F\;-\;V_0^2\,H\,K) \tag{A.39}$$

$$\begin{aligned} D_{51} = {} & 2\,c_i\,u_0\,\cos\phi_i\,C_{M0,i}\;+\;r_{x,i}\,\cos\phi_i\,(2\,u_0\,F\;-\;w_0\,\cos\phi_i\,V_0^2\,K) \\ & -\;r_{z,i}\,(2\,u_0\,E\;+\;w_0\,\cos\phi_i\,V_0^2\,L) \end{aligned} \tag{A.40}$$

$$D_{52} = -V_0^2\,u_0\,\sin\phi_i\,(r_{x,i}\,\cos\phi_i\,K\;+\;r_{z,i}\,L) \tag{A.41}$$

$$\begin{aligned} D_{53} = {} & 2\,c_i\,w_0\,\cos\phi_i\,C_{M0,i}\;+\;r_{x,i}\,\cos\phi_i\,(2\,w_0\,F\;+\;u_0\,\cos\phi_i\,V_0^2\,K) \\ & -\;r_{z,i}\,(2\,w_0\,E\;-\;u_0\,\cos\phi_i\,V_0^2\,L) \end{aligned} \tag{A.42}$$

$$\begin{aligned} D_{54} = {} & 2\,c_i\,r_{y,i}\,w_0\,\cos\phi_i\,C_{M0,i}\;+\;r_{x,i}\,\cos\phi_i\,(2\,w_0\,r_{y,i}\,F\;+\;u_0\,G\,V_0^2\,K) \\ & -\;r_{z,i}\,(2\,w_0\,r_{y,i}\,E\;-\;u_0\,G\,V_0^2\,L) \end{aligned} \tag{A.43}$$

$$\begin{aligned} D_{55} = {} & 2\,c_i\,I\,\cos\phi_i\,C_{M0,i}\;+\;r_{x,i}\,\cos\phi_i\,(2\,I\,F\;-\;J\,\cos\phi_i\,V_0^2\,K) \\ & -\;r_{z,i}\,(2\,I\,E\;+\;J\,\cos\phi_i\,V_0^2\,L) \end{aligned} \tag{A.44}$$

$$\begin{aligned} D_{56} = {} & -\,2\,c_i\,r_{y,i}\,u_0\,\cos\phi_i\,C_{M0,i}\;-\;r_{x,i}\,\cos\phi_i\,(2\,u_0\,r_{y,i}\,F\;-\;H\,V_0^2\,K) \\ & +\;r_{z,i}\,(2\,u_0\,r_{y,i}\,E\;+\;H\,V_0^2\,L) \end{aligned} \tag{A.45}$$

$$\begin{aligned} D_{61} = {} & 2\,c_i\,u_0\,\sin\phi_i\,C_{M0,i}\;+\;r_{x,i}\,\sin\phi_i\,(2\,u_0\,F\;-\;w_0\,\cos\phi_i\,V_0^2\,K) \\ & +\;r_{y,i}\,(2\,u_0\,E\;+\;w_0\,\cos\phi_i\,V_0^2\,L) \end{aligned} \tag{A.46}$$

$$D_{62} = -V_0^2\,u_0\,\sin\phi_i\,(r_{x,i}\,\sin\phi_i\,K\;-\;r_{y,i}\,L) \tag{A.47}$$

$$\begin{aligned} D_{63} = {} & 2\,c_i\,w_0\,\sin\phi_i\,C_{M0,i}\;+\;r_{x,i}\,\sin\phi_i\,(2\,w_0\,F\;+\;u_0\,\cos\phi_i\,V_0^2\,K) \\ & +\;r_{y,i}\,(2\,w_0\,E\;-\;u_0\,\cos\phi_i\,V_0^2\,L) \end{aligned} \tag{A.48}$$

$$\begin{aligned} D_{64} = {} & 2\,c_i\,r_{y,i}\,w_0\,\sin\phi_i\,C_{M0,i}\;+\;r_{x,i}\,\sin\phi_i\,(2\,w_0\,r_{y,i}\,F\;+\;u_0\,G\,V_0^2\,K) \\ & +\;r_{y,i}\,(2\,w_0\,r_{y,i}\,E\;-\;u_0\,G\,V_0^2\,L) \end{aligned} \tag{A.49}$$

$$\begin{aligned} D_{65} = {} & 2\,c_i\,I\,\sin\phi_i\,C_{M0,i}\;+\;r_{x,i}\,\sin\phi_i\,(2\,I\,F\;-\;J\,\cos\phi_i\,V_0^2\,K) \\ & +\;r_{y,i}\,(2\,I\,E\;+\;J\,\cos\phi_i\,V_0^2\,L) \end{aligned} \tag{A.50}$$

$$D_{66} = -2\,c_i\,r_{y,i}\,u_0\,\sin\phi_i\,C_{M0,i} - r_{x,i}\,\sin\phi_i\,(2\,u_0\,r_{y,i}\,F - H\,V_0^2\,K) - r_{y,i}\,(2\,u_0\,r_{y,i}\,E + H\,V_0^2\,L) \tag{A.51}$$

A.1.2 U Matrix Components

$$U_1 = V_0^2\,L\,u_i^2 \tag{A.52}$$
$$U_2 = V_0^2\,\sin\phi_i\,K\,u_i^2 \tag{A.53}$$
$$U_3 = -V_0^2\,\cos\phi_i\,K\,u_i^2 \tag{A.54}$$
$$U_4 = -V_0^2\,G\,K\,u_i^2 \tag{A.55}$$
$$U_5 = V_0^2\,(r_{z,i}\,L + r_{x,i}\,\cos\phi_i\,K)\,u_i^2 \tag{A.56}$$
$$U_6 = V_0^2\,(r_{x,i}\,\sin\phi_i\,K - r_{y,i}\,L)\,u_i^2 \tag{A.57}$$

A.2 Section with Traditional Control Surface

$$w_i = u_0\sin\theta_i + w_0\cos\phi_i\cos\theta_i \tag{A.58}$$
$$u_i = u_0\cos\theta_i - w_0\cos\phi_i\sin\theta_i \tag{A.59}$$
$$V_0^2 = u_0^2 + w_0^2 \tag{A.60}$$
$$\alpha_i = \frac{w_i}{u_i} \tag{A.61}$$
$$A = C_{L0,i} + C_{L\delta,i}\,\delta_0 + \alpha_i\,(C_{D0,i} + C_{L\alpha,i}) \tag{A.62}$$
$$B = C_{D0,i} - \alpha_i\,(C_{L0,i} + C_{L\alpha,i}\,\alpha_i + C_{L\delta,i}\,\delta_0) \tag{A.63}$$
$$C = 2\,C_{L\alpha,i}\,w_i + (C_{L0,i} + C_{L\delta,i}\,\delta_0)\,u_i \tag{A.64}$$
$$E = B\,\cos\theta_i + A\,\sin\theta_i \tag{A.65}$$
$$F = A\,\cos\theta_i - B\,\sin\theta_i \tag{A.66}$$
$$G = r_{y,i}\cos\phi_i + r_{z,i}\sin\phi_i \tag{A.67}$$
$$H = r_{y,i}\,w_0\cos\phi_i - r_{x,i}\,u_0\sin\phi_i \tag{A.68}$$
$$I = r_{z,i}\,u_0 - r_{x,i}\,w_0 \tag{A.69}$$
$$J = r_{x,i}\,u_0 + r_{z,i}\,w_0 \tag{A.70}$$
$$K = \frac{C\sin\theta_i}{u_i^3} + (C_{D0,i} + C_{L\alpha,i})\frac{\cos\theta_i}{u_i^2} \tag{A.71}$$

$$L = \frac{C \cos\theta_i}{u_i^3} \; - \; (C_{D0,i} \; + \; C_{L\alpha,i}) \frac{\sin\theta_i}{u_i^2} \tag{A.72}$$

A.2.1 D Matrix Components

$$D_{11} = \; - \, (2\, u_0\, E \; + \; w_0 \; \cos\phi_i \, V_0^2 \, L) \tag{A.73}$$

$$D_{12} = \; - \, u_0 \; \sin\phi_i \, V_0^2 \, L \tag{A.74}$$

$$D_{13} = \; - \, (2\, w_0\, E \; - \; u_0 \; \cos\phi_i \, V_0^2 \, L) \tag{A.75}$$

$$D_{14} = \; - \, (2\, r_{y,i}\, w_0\, E \; - \; u_0\, G\, V_0^2 \, L) \tag{A.76}$$

$$D_{15} = \; - \, (2\, I\, E \; + \; J \; \cos\phi_i \, V_0^2 \, L) \tag{A.77}$$

$$D_{16} = 2\, r_{y,i}\, u_0\, E \; + \; H\, V_0^2 \, L \tag{A.78}$$

$$D_{21} = \sin\phi_i \, (2\, u_0\, F \; - \; w_0 \; \cos\phi_i \, V_0^2 \, K) \tag{A.79}$$

$$D_{22} = \; - \, u_0 \; \sin\phi_i^2 \, V_0^2 \, K \tag{A.80}$$

$$D_{23} = \sin\phi_i \, (2\, w_0\, F \; + \; u_0 \; \cos\phi_i \, V_0^2 \, K) \tag{A.81}$$

$$D_{24} = \sin\phi_i \, (2\, r_{y,i}\, w_0\, F \; + \; u_0\, G\, V_0^2 \, K) \tag{A.82}$$

$$D_{25} = \sin\phi_i \, (2\, I\, F \; - \; J \; \cos\phi_i \, V_0^2 \, K) \tag{A.83}$$

$$D_{26} = \; - \; \sin\phi_i \, (2\, r_{y,i}\, u_0\, F \; - \; H\, V_0^2 \, K) \tag{A.84}$$

$$D_{31} = \; - \; \cos\phi_i \, (2\, u_0\, F \; - \; w_0 \; \cos\phi_i \, V_0^2 \, K) \tag{A.85}$$

$$D_{32} = u_0 \; \cos\phi_i \; \sin\phi_i \, V_0^2 \, K \tag{A.86}$$

$$D_{33} = \; - \; \cos\phi_i \, (2\, w_0\, F \; + \; u_0 \; \cos\phi_i \, V_0^2 \, K) \tag{A.87}$$

$$D_{34} = \; - \; \cos\phi_i \, (2\, r_{y,i}\, w_0\, F \; + \; u_0\, G\, V_0^2 \, K) \tag{A.88}$$

$$D_{35} = \; - \; \cos\phi_i \, (2\, I\, F \; - \; J \; \cos\phi_i \, V_0^2 \, K) \tag{A.89}$$

$$D_{36} = \cos\phi_i \, (2\, r_{y,i}\, u_0\, F \; - \; H\, V_0^2 \, K) \tag{A.90}$$

$$D_{41} = \; - \, G \, (2\, u_0\, F \; - \; w_0 \; \cos\phi_i \, V_0^2 \, K) \tag{A.91}$$

$$D_{42} = V_0^2 \, u_0 \; \sin\phi_i \, G\, K \tag{A.92}$$

$$D_{43} = \; - \, G \, (2\, w_0\, F \; + \; u_0 \; \cos\phi_i \, V_0^2 \, K) \tag{A.93}$$

$$D_{44} = \; - \, G \, (2\, w_0\, r_{y,i}\, F \; + \; u_0\, G\, V_0^2 \, K) \tag{A.94}$$

$$D_{45} = \; - \, G \, (2\, I\, F \; - \; \cos\phi_i \, V_0^2 \, J\, K) \tag{A.95}$$

$$D_{46} = G \, (2\, u_0\, r_{y,i}\, F \; - \; V_0^2 \, H\, K) \tag{A.96}$$

$$
\begin{aligned}
D_{51} &= 2\,c_i\,u_0\,\cos\phi_i\,(C_{M0,i} + C_{M\delta,i}\,\delta_0) \\
&\quad + r_{x,i}\,\cos\phi_i\,(2\,u_0\,F - w_0\,\cos\phi_i\,V_0^2\,K) \\
&\quad - r_{z,i}\,(2\,u_0\,E + w_0\,\cos\phi_i\,V_0^2\,L)
\end{aligned} \tag{A.97}
$$

$$
D_{52} = -V_0^2\,u_0\,\sin\phi_i\,(r_{x,i}\,\cos\phi_i\,K + r_{z,i}\,L) \tag{A.98}
$$

$$
\begin{aligned}
D_{53} &= 2\,c_i\,w_0\,\cos\phi_i\,(C_{M0,i} + C_{M\delta,i}\,\delta_0) \\
&\quad + r_{x,i}\,\cos\phi_i\,(2\,w_0\,F + u_0\,\cos\phi_i\,V_0^2\,K) \\
&\quad - r_{z,i}\,(2\,w_0\,E - u_0\,\cos\phi_i\,V_0^2\,L)
\end{aligned} \tag{A.99}
$$

$$
\begin{aligned}
D_{54} &= 2\,c_i\,r_{y,i}\,w_0\,\cos\phi_i\,(C_{M0,i} + C_{M\delta,i}\,\delta_0) \\
&\quad + r_{x,i}\,\cos\phi_i\,(2\,w_0\,r_{y,i}\,F + u_0\,G\,V_0^2\,K) \\
&\quad - r_{z,i}\,(2\,w_0\,r_{y,i}\,E - u_0\,G\,V_0^2\,L)
\end{aligned} \tag{A.100}
$$

$$
\begin{aligned}
D_{55} &= 2\,c_i\,I\,\cos\phi_i\,(C_{M0,i} + C_{M\delta,i}\,\delta_0) \\
&\quad + r_{x,i}\,\cos\phi_i\,(2\,I\,F - J\,\cos\phi_i\,V_0^2\,K) \\
&\quad - r_{z,i}\,(2\,I\,E + J\,\cos\phi_i\,V_0^2\,L)
\end{aligned} \tag{A.101}
$$

$$
\begin{aligned}
D_{56} &= -2\,c_i\,r_{y,i}\,u_0\,\cos\phi_i\,(C_{M0,i} + C_{M\delta,i}\,\delta_0) \\
&\quad - r_{x,i}\,\cos\phi_i\,(2\,u_0\,r_{y,i}\,F - H\,V_0^2\,K) \\
&\quad + r_{z,i}\,(2\,u_0\,r_{y,i}\,E + H\,V_0^2\,L)
\end{aligned} \tag{A.102}
$$

$$
\begin{aligned}
D_{61} &= 2\,c_i\,u_0\,\sin\phi_i\,(C_{M0,i} + C_{M\delta,i}\,\delta_0) \\
&\quad + r_{x,i}\,\sin\phi_i\,(2\,u_0\,F - w_0\,\cos\phi_i\,V_0^2\,K) \\
&\quad + r_{y,i}\,(2\,u_0\,E + w_0\,\cos\phi_i\,V_0^2\,L)
\end{aligned} \tag{A.103}
$$

$$
D_{62} = -V_0^2\,u_0\,\sin\phi_i\,(r_{x,i}\,\sin\phi_i\,K - r_{y,i}\,L) \tag{A.104}
$$

$$
\begin{aligned}
D_{63} &= 2\,c_i\,w_0\,\sin\phi_i\,(C_{M0,i} + C_{M\delta,i}\,\delta_0) \\
&\quad + r_{x,i}\,\sin\phi_i\,(2\,w_0\,F + u_0\,\cos\phi_i\,V_0^2\,K) \\
&\quad + r_{y,i}\,(2\,w_0\,E - u_0\,\cos\phi_i\,V_0^2\,L)
\end{aligned} \tag{A.105}
$$

$$
\begin{aligned}
D_{64} &= 2\,c_i\,r_{y,i}\,w_0\,\sin\phi_i\,(C_{M0,i} + C_{M\delta,i}\,\delta_0) \\
&\quad + r_{x,i}\,\sin\phi_i\,(2\,w_0\,r_{y,i}\,F + u_0\,G\,V_0^2\,K) \\
&\quad + r_{y,i}\,(2\,w_0\,r_{y,i}\,E - u_0\,G\,V_0^2\,L)
\end{aligned} \tag{A.106}
$$

$$
\begin{aligned}
D_{65} &= 2\,c_i\,I\,\sin\phi_i\,(C_{M0,i} + C_{M\delta,i}\,\delta_0) \\
&\quad + r_{x,i}\,\sin\phi_i\,(2\,I\,F - J\,\cos\phi_i\,V_0^2\,K) \\
&\quad + r_{y,i}\,(2\,I\,E + J\,\cos\phi_i\,V_0^2\,L)
\end{aligned} \tag{A.107}
$$

$$
\begin{aligned}
D_{66} = & -2\,c_i\,r_{y,i}\,u_0\,\sin\phi_i\,(C_{M0,i} + C_{M\delta,i}\,\delta_0) \\
& - r_{x,i}\,\sin\phi_i\,(2\,u_0\,r_{y,i}\,F - H\,V_0^2\,K) \\
& - r_{y,i}\,(2\,u_0\,r_{y,i}\,E + H\,V_0^2\,L)
\end{aligned} \tag{A.108}
$$

A.2.2 U Matrix Components

$$U_1 = \frac{w_0\,\cos\phi_i\,V_0^2\,C_{L\delta,i}}{u_i} \tag{A.109}$$

$$U_2 = \frac{u_0\,\sin\phi_i\,V_0^2\,C_{L\delta,i}}{u_i} \tag{A.110}$$

$$U_3 = -\frac{u_0\,\cos\phi_i\,V_0^2\,C_{L\delta,i}}{u_i} \tag{A.111}$$

$$U_4 = -\frac{u_0\,V_0^2\,G\,C_{L\delta,i}}{u_i} \tag{A.112}$$

$$U_5 = \cos\phi_i\,V_0^2\,\left(\frac{C_{L\delta,i}\,C}{u_i} + C_{M\delta,i}\,c_i\right) \tag{A.113}$$

$$U_6 = V_0^2\,\left(C_{M\delta,i}\,c_i\,\sin\phi_i - \frac{C_{L\delta,i}\,H}{u_i}\right) \tag{A.114}$$

References

[1] "3D-printed drone aircraft takes to the sky at Sheffield". In: *Electronics Weekly* 2583 (Apr. 2014). URL: http://ezaccess.libraries.psu.edu/login?url=https://search-proquest-com.ezaccess.libraries.psu.edu/docview/1522270261?accountid=13158.

[2] Patrick C. Murphy et al. *System Identification Applied to Dynamic CFD Simulation and Wind Tunnel Data*. 2011. URL: https://ntrs.nasa.gov/archive/nasa/casi.ntrs.nasa.gov/20110014614.pdf.

[3] John D. Anderson. *Fundamentals of Aerodynamics*. Fifth. McGraw-Hill, 2011.

[4] *ArduPilot*. 2017. URL: ardupilot.org.

[5] D.J. Auld and K. Srinivas. *Aerodynamics for Students. Blade Element Propeller Analysis*. Department of Aerospace, Mechanical & Mechatronic Engineering, University of Sydney. 2006. URL: http://www-mdp.eng.cam.ac.uk/web/library/enginfo/aerothermal_dvd_only/aero/contents.html.

[6] ConceptLaser. *X Line 2000R*. 2017. URL: https://www.concept-laser.de/en/products/machines.html.

[7] Mark Drela and Harold Youngren. *AVL*. Version 3.35. 2017. URL: web.mit.edu/drela/Public/web/avl/.

[8] Mark Drela and Harold Youngren. *XFOIL*. Version 6.99. 2013. URL: web.mit.edu/drela/Public/web/xfoil/.

[9] Bernard Etkin and Lloyd D. Reid. *Dynamics of Flight, Stability and Control*. 3rd. John Wiley and Sons, Inc., 1996.

[10] F. Forte et al. “Control of modular aerial robots: Combining under- and fully-actuated behaviors”. In: *2012 IEEE 51st IEEE Conference on Decision and Control (CDC)*. Dec. 2012, pp. 1160–1165. DOI: 10.1109/CDC.2012.6425886.

[11] 3D Hubs. *2017 3D Printers Guide*. 2017. URL: https://www.3dhubs.com/best-3d-printer-guide.

[12] MakerBot. *Replicator Mini+*. 2017. URL: https://www.makerbot.com/replicator-mini/.

[13] Bridget Butler Millsaps. *Airbus Officially Unveils Thor, the Fully 3D Printed Plane that Flies Beautifully*. 2016. URL: https://3dprint.com/137389/airbus-thor-3d-printed-plane/.

[14] Sanghyuk Park. “Modeling with vortex lattice method and frequency sweep flight test for a fixed-wing {UAV}”. In: *Control Engineering Practice* 21.12 (2013), pp. 1767–1775. ISSN: 0967-0661. DOI: https://doi.org/10.1016/j.conengprac.2013.09.002. URL: http://www.sciencedirect.com/science/article/pii/S0967066113001640.

[15] *Pixhawk*. 2017. URL: http://pixhawk.org.

[16] *PX4: The Professional Autopilot*. 2017. URL: px4.io.

[17] GE Global Research. *3D Printing Creates New Parts for Aircraft Engines*. 2016. URL: http://www.geglobalresearch.com/innovation/3d-printing-creates-new-parts-aircraft-engines.

[18] 3D Printing from Scratch. *Types of 3D Printers*. 2017. URL: http://3dprintingfromscratch.com/common/types-of-3d-printers-or-3d-printing-technologies-overview/#.

[19] Michael S. Selig. “Real-Time Flight Simulation of Highly Maneuverable Unmanned Aerial Vehicles”. In: *Journal of Aircraft* (2014).

[20] Brian L. Stevens and Frank L. Lewis. *Aircraft Control and Simulation*. Second. John Wiley and Sons, Inc., 2003.

[21] Stratasys. *Fortus 900mc*. 2017. URL: http://www.stratasys.com/3d-printers/production-series/fortus-900mc.

[22] J. Zhang et al. “Immersion and invariance based nonlinear adaptive longitudinal control for autonomous aircraft”. In: *2011 9th World Congress on Intelligent Control and Automation*. June 2011, pp. 985–989. DOI: 10.1109/WCICA.2011.5970663.